The high-altitude peaks of atmospheric ozone as observed by NOMAD/UVIS onboard the ExoMars Trace Gas Orbiter Mission

Alain SJ. Khayat[1,2,*], Michael D. Smith[1], Michael Wolff[3], Frank Daerden[4], Lori Neary[4], Manish R. Patel[5], Arianna Piccialli[4], Ann C. Vandaele[4], Ian Thomas[4], Bojan Ristic[4], Jon Mason[5], Yannick Willame[4], Cedric Depiesse[4], Giancarlo Bellucci[6], José Juan López-Moreno[7], and the NOMAD team.

[1] Solar System Exploration Division, Planetary Systems Laboratory Code 693, NASA Goddard Space Flight Center, Greenbelt, MD 20771, United States.
[2] Center for Research and Exploration in Space Science & Technology (CRESST II), Department of Astronomy, University of Maryland, College Park, MD 20742, United States.
[3] Space Science Institute, Boulder, Colorado, USA.
[4] Royal Belgian Institute for Space Aeronomy BIRA-IASB, Brussels, Belgium.
[5] School of Physical Sciences, The Open University, Milton Keynes, UK.
[6] Instituto di Astrofisica e Planetologia Spaziali, IAPS ‑ INAF, Rome, Italy.
[7] Instituto de Astrofisica de Andalucia, IAA ‑ CSIC, Glorieta de la Astronomia, Granada, Spain.

[*]Corresponding author: Alain SJ. Khayat (alain.khayat@nasa.gov)
Solar System Exploration Division, Planetary Systems Laboratory Code 693, NASA Goddard Space Flight Center, Greenbelt, MD 20771.
(301) 614-5420.

Key Points:

- We provide the detection of a high-altitude peak of ozone between 40 and 60 km in altitude over the north polar latitudes of Mars.
- We confirm the presence of a previously detected, more prominent high-altitude ozone peak in the south polar latitudes.
- Both high-altitude peaks are observed in the sunrise and sunset occultations, indicating that the layers could persist during the day.

Abstract

Solar occultations performed by the Nadir and Occultation for MArs Discovery (NOMAD) ultraviolet and visible spectrometer (UVIS) onboard the ExoMars Trace Gas Orbiter (TGO) have provided a comprehensive mapping of ozone density, describing the seasonal and spatial distribution of atmospheric ozone in detail. The observations presented here extend over a full Mars year between April 2018 at the beginning of the TGO science operations during late northern summer on Mars (L_s = 163°) and March 2020. UVIS provided transmittance spectra of the martian atmosphere in the 200 - 650 nm wavelength range, allowing measurements of the vertical distribution of the ozone density using its Hartley absorption band (200 – 300 nm). Our findings indicate the presence of (1) a high-altitude peak of ozone between 40 and 60 km in altitude over the north polar latitudes for over 45 % of the martian year, particularly during mid-northern spring, late northern summer-early southern spring, and late southern summer, and (2) a second, but more prominent, high-altitude ozone peak in the south polar latitudes, lasting for over 60 % of the year including the southern autumn and winter seasons. When they are present, both high-altitude peaks are observed in the sunrise and sunset occultations, indicating that the layers could persist during the day. Model results from the GEM-Mars General Circulation predicts the general behavior of the high-altitude peaks of ozone observed by UVIS and are used in an attempt to further our understanding of the chemical processes controlling the high-altitude ozone on Mars.

1. Introduction

The presence of ozone (O_3) in the martian atmosphere has been observed since it was first detected by the ultraviolet spectrometer experiments on the 1969 and 1971 Mariner flyby missions (Barth and Hord, 1971; Barth et al., 1972; 1973). Ozone is sensitive to changes in the incoming solar ultraviolet (UV) flux on the planet. It is mainly formed by the three-body reaction involving molecular (O_2) and atomic oxygen (O) that are byproducts of the photolysis of CO_2, the main atmospheric constituent on Mars (molar fraction ~ 95%). In the opposite direction, ultraviolet radiation during the day destroys O_3 back to O, O_2 and $O_2(^1\Delta_g)$. The abundance of ozone is regulated locally by the presence of the odd hydrogen species (H, OH and HO_2) produced by the photolysis of water vapor (H_2O). The odd hydrogen species play a major role in regenerating the photo-dissociated CO_2 in the upper atmosphere, therefore helping to stabilize the martian atmosphere (e.g., Lefèvre at al., 2004; Perrier et al., 2006).

The periodic monitoring of O_3 on Mars includes observations from the ground and from space using flyby missions, Mars orbiting satellites, and space telescopes. Due to the presence of telluric O_3 that renders the terrestrial atmosphere opaque, ground-based observations have used heterodyne infrared spectroscopy to measure total column abundances of O_3 from its Doppler-shifted absorption lines around 9.7 μm (Espenak et al., 1991; Fast et al., 2006). The observations provided a confirmation of the odd hydrogen activity that predicts anticorrelation of ozone and water vapor abundances (e.g., Clancy & Nair, 1996; Clancy et al., 2016). Indirect observations of O_3 from the ground (Noxon et al., 1976; Novak et al., 2002) targeted the $O_2(^1\Delta_g)$ produced by the photolysis of ozone, as it is characterized by an emission band system around 1.27 µm tracing the presence and abundance of ozone in the middle atmosphere (~ 25 km).

Space-based observations of Mars include UV observations of the Hartley band (200 – 300 nm) of ozone by the Faint Object Spectrograph onboard the Hubble Space Telescope at $L_s = 63.5°$ during Mars' late northern spring (Clancy et al., 1996). The measurements show low-latitude O_3 abundances that are significantly elevated (≥ 100 %) compared to the ones taken during northern fall ($L_s = 208°$) by Espenak et al. (1991). This large increase is consistent with photochemical models due to large annual variations in the photochemistry on Mars (Clancy & Nair, 1996).

Global distributions of ozone column abundance were made possible using continuous UV observations of Mars by the Mars Reconnaissance Orbiter (Clancy et al., 2016) and Mars Express (Perrier et al., 2006). The Mars Color Imager (MARCI) on MRO included a pair of UV imaging channels centered within (260 nm) and outside (320 nm) the O_3 Hartley band (Malin et al., 2001; 2008). This imaging system allowed daytime (local time of 3 PM) measurements of the total column abundance of O_3 using its absorption against the solar UV radiation reflected from the surface of Mars and atmospheric scattering. The observations by Clancy et al. (2016) provided daily global mapping of ozone between Mars Year (MY) 28 and MY 32, showing elevated abundances at high northern and southern latitudes over the fall-winter-spring seasons, as well as at low latitudes around Mars aphelion ($L_s = 71°$).

Dayside observations with UV spectroscopy by the Spectroscopy for the Investigation of the Characteristics of the Atmosphere of Mars (SPICAM) instrument onboard Mars Express also provided distribution of the total column concentration of O_3 from nadir spectra in the 110 – 320 nm range (Perrier et al., 2006). The reported observations extended between January 2004 and April 2006, covering a full Mars year between $L_s = 331°$ of MY 26 and $L_s = 37°$ of MY 28. When compared to General Circulation Models (GCM, Lefèvre at al., 2004), the behavior of ozone is in good overall agreement showing high variability at the northern high latitudes around late winter-early spring, and an increase in O_3 around the equator during the aphelion season. However, GCM predictions underestimated the column abundance of O_3 at high latitudes in both hemispheres during northern spring (southern autumn) when compared to the retrieved SPICAM values. Willame et al. (2018) tracked the seasonal evolution of the ozone column using SPICAM data between late MY 26 and the end of MY 30. Large ozone abundances were observed over the winter poles with the condensation of atmospheric water, also seen by previous observations including those by SPICAM (Perrier et al., 2006) and MARCI (Clancy et al., 2016).

The vertical distribution of ozone in the atmosphere is very diagnostic in delineating the role that photochemistry plays at the different levels in the atmosphere at various seasons. The earliest attempts to provide vertical profiles from solar occultations yielded the first detection of O_3 in the middle atmosphere of Mars using the *Phobos* 2 spacecraft, with values nearing 10^8 molecules/cm^3 (Blamont et al., 1993). On the other hand, stellar occultations to retrieve vertical profiles and probe the evolution of ozone during nighttime on Mars were performed by SPICAM (Lebonnois et al., 2006). The observations covered latitudes between 30°S and 60°N during early northern spring (L_s= 8° - 50°) and autumn (L_s = 155° - 270°), and the southern hemisphere during southern autumn and winter (L_s= 20° and 155°).

These nighttime observations from stellar occultations were limited in frequency and coverage but provided initial clues to the presence of a near-surface ozone layer below 30 km and a nocturnal layer in the altitude range 20 - 50 km, later confirmed by Lefèvre et al. (2007). The presence of ozone near the surface is expected due to solar UV radiation screening by CO_2 which limits the solar UV radiation that photolyzes O_3 and inhibits the presence of the hydroxyl radicals (HO_x) produced by H_2O photolysis (e.g., Daerden et al., 2019). The ozone enhancement peaks in the dry polar winter regions where atmospheric water vapor is suppressed near the ground (e.g., Lefèvre at al., 2004; Daerden et al., 2019). The ozone layer between 20 and 50 km is expected to form at night after the removal of O_3 by the solar UV radiation during the day, and then its re-generation after sunset (Lebonnois et al., 2006). The results from SPICAM show an increase in the O_3 abundance in the nocturnal layer before L_s= 40° around mid and low latitudes, reaching peak abundances 6–9 × 10^9 molecules/cm^3 around altitude 40 km, before dissipating by L_s= 130°. However, these stellar occultations were limited to nighttime, and the solar occultation observations presented here are needed to track the evolution of this layer.

Three-dimensional photochemistry models have been used to investigate the behavior of the vertical distribution of ozone (Montmessin & Lefèvre, 2013; Daerden et al., 2019). In particular, Montmessin & Lefèvre (2013) discussed the ozone enhancement seen by earlier analyses of the SPICAM data (Lebonnois et al., 2006) that appeared at 50 km in the southern hemisphere above the winter pole, with no apparent counterpart over the north pole. They showed that the O_3 formation process is more efficient in the south where oxygen-rich air is largely transported from sunlit regions all the way to the polar regions, leading to the formation of ozone at night when oxygen atoms recombine.

However, Daerden et al. (2019) have more recently presented a more complete picture of the vertical distribution of O_3 on Mars using the GEM-Mars general circulation model (GEM-Mars), which predicts the formation of a high-altitude layer of O_3 at 40 - 60 km in altitude between 60°N and 90°N, lasting between L_s= 170° and L_s= 30° of the following year, with minimum abundances in O_3 reached at L_s= 270°.

The existence of ozone datasets that encompass the full seasonal cycle, as well as more complete latitudinal and vertical coverage, would be extremely valuable for understanding photochemistry in the martian atmosphere and for further improving the existing photochemical models. In this work we take advantage of the ExoMars Trace Gas Orbiter NOMAD/UVIS solar occultation observations for a full Mars year to focus on characterization of the high-altitude peak of ozone, tracking its latitudinal, vertical, local time (LT), and seasonal dependencies. This work is undertaken in parallel to a companion study performed using the same observations from the NOMAD/UVIS instrument (Patel et al., this issue). A comparison of the results from the two studies is provided in the supplementary material, showing that both datasets are in general agreement (Figs. S1-S2).

In Section 2, we describe the NOMAD instrument, the solar occultation observations used in this work, and we present the transmittance spectra at various altitudes in the martian atmosphere showing the Hartley band absorption of ozone. In Section 3 we provide details on the retrieval process that derives vertical density profiles of O_3 from line-of-sight opacities through the atmosphere and we explain the error analysis in the retrieval process. In section 4 we describe the GEM-Mars model. The retrieval results tracking the presence of the high-altitude peak of ozone and their comparison with GEM-Mars model outputs are presented in Section 5, and we finally discuss and summarize the findings of this work in Section 6.

2. Data Set: Spacecraft, instrument and observations

2.1. NOMAD Instrument

The ExoMars Trace Gas Orbiter (TGO) has been returning data from Mars since April 21, 2018. The spacecraft is in a near-circular orbit with an inclination of 74°, orbiting Mars every ~2 hours at an average distance of 400 km from the surface of the planet with a precessing orbit that covers different local times (Vandaele et al., 2018). The Nadir and Occultation for MArs Discovery (NOMAD) is a spectrometer suite onboard TGO, providing observations in the nadir, limb, and solar occultation (SO) modes.

The wavelength coverage of NOMAD is in the near-infrared range with the SO spectrometer (2.3 μm – 4.3 μm) and the Limb Nadir Solar Occultation (LNO, 2.3 μm – 3.8 μm). It also covers portions of the ultraviolet-visible range with the ultraviolet and visible spectrometer UVIS between 200 nm and 650 nm (Patel et al., 2017).

UVIS is a single spectrometer unit within NOMAD that is capable of receiving light from two separate telescopes, one for the nadir mode and another for the solar occultation mode where the incoming light is directed using a periscope (Patel et al., 2017). This dual-telescope setup then feeds light via a selection mechanism into a single spectrometer that provides a spectral resolution of Δλ = 1.2 – 1.6 nm in the registered spectrum on a detector array of 1024 × 256 pixels. The field of view (FOV) of UVIS is a circular aperture covering 2 arcminutes in the sky. A more detailed description of the design and performance of UVIS can be found in Vandaele et al (2015) and Patel et al (2017).

2.2 UVIS solar occultation observations

The solar occultation observations covered in this study extend over a full Mars year (687 Earth days) from MY 34 at L_s = 163° to MY 35 at the same L_s, corresponding to April 21, 2018 and March 9, 2020, respectively. These solar occultations cover latitudes between 89 °N and 84 °S, with ~4100 observations in total. The seasonal coverage for the full Mars year at the different latitudes and local times is shown in Figure 1. The beginning of the observations corresponds to the middle of the plot at L_s = 163° and extends to L_s = 360° at the end of MY 34, whereas L_s = 0° - 163° belongs to following MY 35.

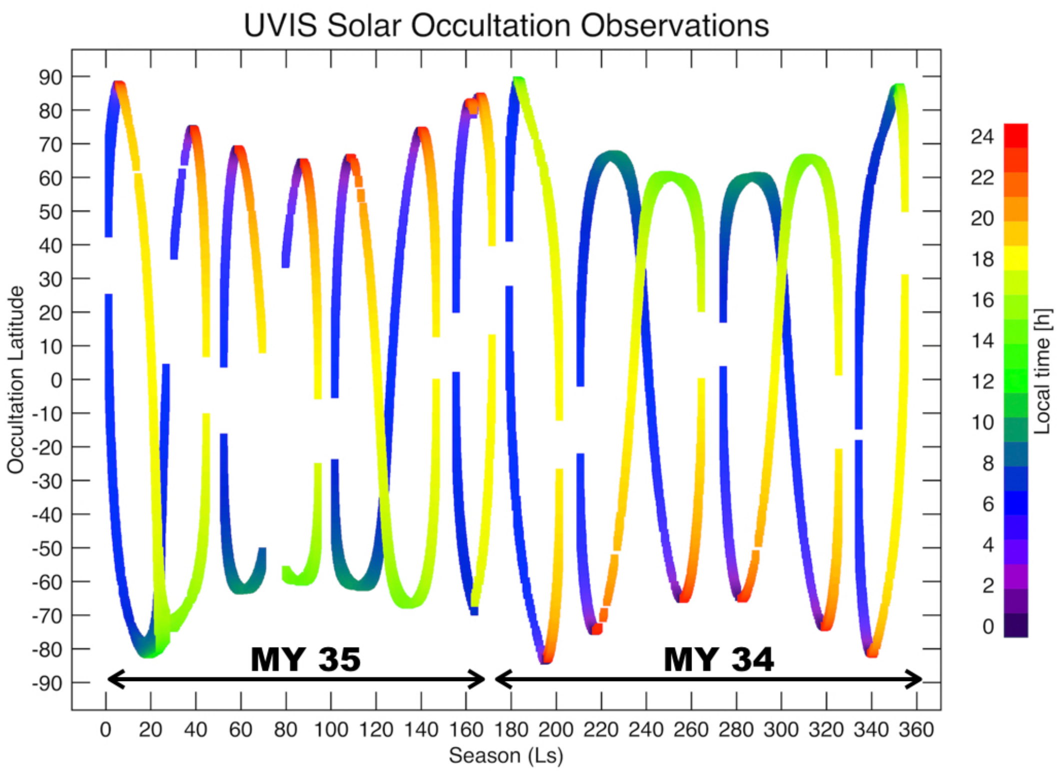

Figure 1. The seasonal (L_s), latitudinal, and local time distribution of the UVIS observations used in this work. The middle of the plot at L_s = 163° corresponds to the beginning of the observations on April 22, 2018 in MY 34. The gaps in the observations are mostly due to the orbital configuration that doesn't allow solar occultations when UVIS is pointed directly to the sun during an entire TGO orbit. Most of the local times covered during the occultations are before LT 10:00 h and after 18:00 h. We made use of observations to retrieve the vertical distribution of atmospheric ozone on Mars for a full Martian year at a vertical resolution < 1km.

The atmosphere is typically sampled up to twice during each orbit at the ingress (sunset) and egress (sunrise) configurations from the surface up to 200 km in altitude at vertical resolutions < 1 km. However, the orbital inclination of TGO does not allow solar occultations to be continuously performed when the "beta" angle between the orbital plane of the spacecraft and the vector pointing towards the sun exceeds 67° (Vandaele et al., 2018). This angle defines how frequently the different latitudes on Mars are being sounded by UVIS. In this study, 20% of the observations cover the equatorial latitudes ± 30°, 45% cover the mid-latitudes 30 °N - 60 °N and 30 °S - 60 °S, and 35% cover latitudes poleward of 60 °N and 60 °S.

As the spacecraft passes behind the planet during an ingress and reemerges during egress, the solar radiance is attenuated by the atmosphere along the instrument's line-of-sight, therefore providing information on the atmospheric composition at different altitudes.

2.3 UVIS solar occultation spectra

Figure 2 represents typical solar occultation spectra at different tangent altitudes, spanning the range from the surface of Mars to the top of the atmosphere (i.e., where the transmittance is unity). These data are taken from the region of UVIS wavelength range used for the work we present here, i.e., between 220 nm and 370 nm.

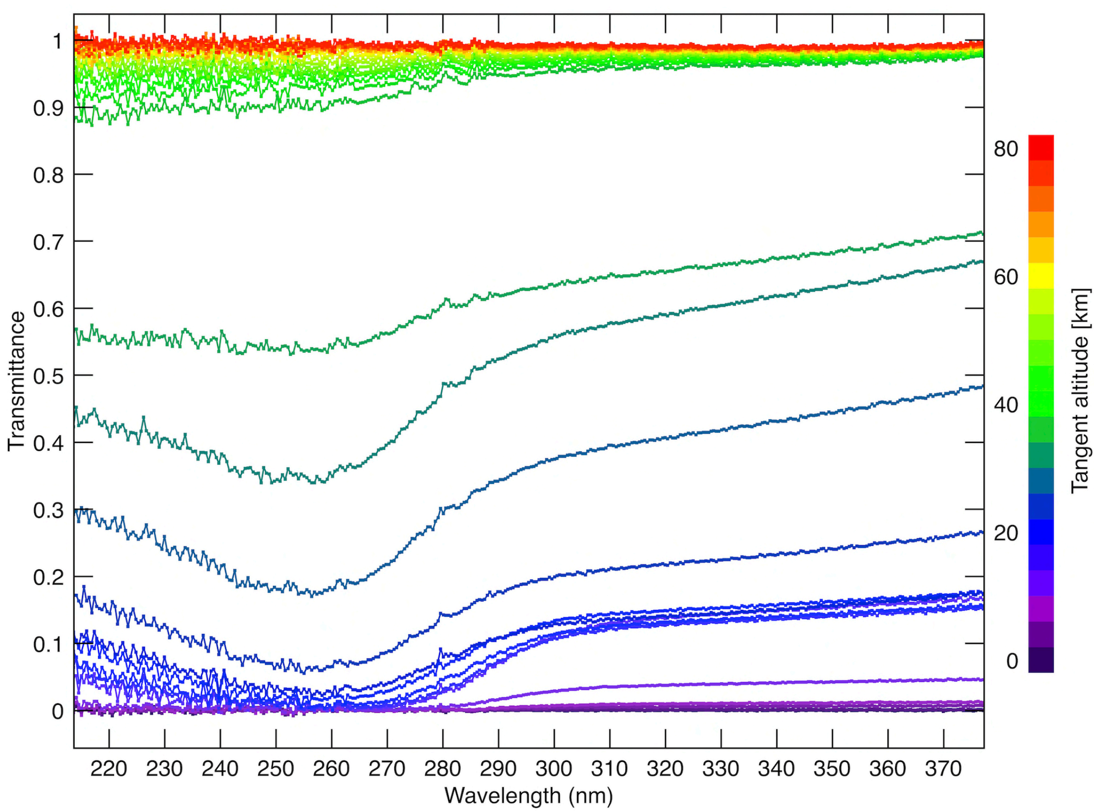

Figure 2. Typical UVIS atmospheric transmittance spectra from solar occultation observation 20180503_012553_1p0b_UVIS_E taken on May 3, 2018 around the beginning of the TGO science phase at L_s = 169° at mean occultation latitude 74.9 °N and mean longitude -87.1 °E, spanning LT = 19.0 and

19.3 h. A reference solar spectrum is taken outside the atmosphere, and the transmittance spectra are obtained by ratioing the solar occultation spectra to the reference spectrum. As indicated by the color bar, high transmittance spectra belong to the upper parts of the atmosphere whereas low transmittance spectra belong to the lower parts close to the surface of Mars indicating more atmospheric absorption. The prominent absorption that is centered around 250 nm belongs to the ozone Hartley band, used to retrieve the abundance of O_3.

Each transmittance spectrum is obtained by dividing the solar radiation through the martian atmosphere as received at UVIS by the solar irradiance at UVIS of a reference spectrum outside the atmosphere. The spectra in the observations were taken around late northern spring (L_s = 169°) above northern latitudes between 71.3 °N and 78.5 °N and longitudes between -91.0 °E and -81.9 °E, between LT= 19.0 h and 19.3 h. The transmittance spectra clearly show the presence of the Hartley absorption band of O_3 at 250 nm (220 nm – 300 nm), and the overall continuum level set by the absorption of suspended dust aerosols in the martian atmosphere. The atmospheric opacity, typically dominated by dust aerosols, increasingly attenuates the signal at the lowest altitudes before the signal is completely lost close to the surface. The signal-to-noise ratio (SNR) in the spectra follows the transmittance. In the continuum around 300 – 330 nm outside the O_3 band, the measured SNR varies between ~ 750 at 65 km down to ~ 140 at 20 km. We made use of such observations to provide the seasonal distribution of the vertical abundance of atmospheric O_3 across Mars.

3. Ozone retrieval process

3.1 Retrieval algorithm

During a solar occultation, UVIS measures the solar radiance after being modified by extinction from the martian atmosphere along the line-of-sight (LOS):

$$I_\lambda(UVIS) = I_\lambda(solar) \times T_\lambda. \quad (1)$$

where $I_\lambda(UVIS)$ is the measured intensity at UVIS at wavelength λ, $I_\lambda(solar)$ is the solar irradiance at top of the atmosphere, $T_\lambda = e^{-\tau_\lambda}$ is the transmittance (Fig. 2), and τ_λ is the integrated optical depth along the atmospheric slant path at each tangent altitude above the areoid of Mars.

The transmittance spectra in the UVIS wavelength coverage longward of 200 nm are mostly impacted by O_3 and aerosol optical depths, as absorption from CO_2, the main atmospheric constituent in the martian atmosphere becomes negligible above 180 nm (Perrier et al., 2006). The slant optical depth of O_3 can be expressed as:

$$\tau_\lambda^{O_3} = \int n_{O_3} \times \sigma_\lambda^{O_3} \times ds, \quad (2)$$

where n_{O_3} is the number density of ozone (molecules/cm^3), $\sigma_\lambda^{O_3}$ (cm^2/molecule) is the wavelength-dependent absorption cross section of the Hartley band (Sander et al., 2011), and *ds* is the increment in the atmospheric path length (cm).

Figure 3 (left panel) shows the occultation spectra in opacity space $\tau_\lambda = -\ln(T_\lambda)$ for the same observation in Fig. 2 with an upper limit τ_λ = 4.6 (or T_λ > 0.01) that is specified in the retrieval process. This limit is set where the transmittance (and the corresponding SNR) become too small to be useful for the retrieval of ozone. The lowest altitude in the retrieval process is defined at this opacity boundary.

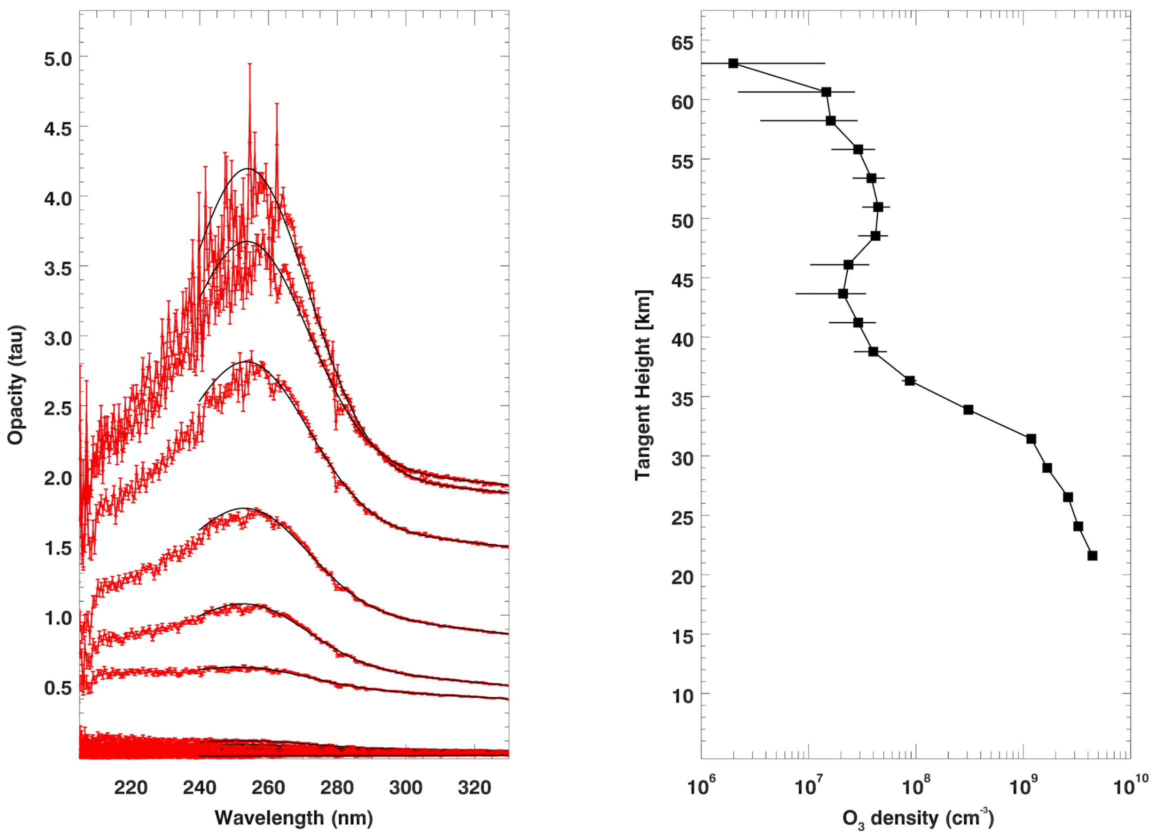

Figure 3. Left panel: A portion of typical UVIS spectra from observation 20180503_012553_1p0b_UVIS_E shown in Fig. 2. The spectra are shown in optical depth space ($\tau = -ln[T_r]$). The spectral feature caused by the O_3 Hartley band centered around 250 nm is shown. The portion used in the retrieval is between 240 and 330 nm and the best fit computed spectrum (black) are compared against the UVIS observation (red). Right panel: The retrieved vertical distribution of ozone density as retrieved from the spectra in the left panel. Retrieved values for O_3 at tangent altitudes 20 km and 56 km are 3×10^9 and 2×10^7 molecules/cm^3, respectively.

In order to retrieve the vertical distribution of ozone in the atmosphere using optical depths along the LOS at each tangent altitude, we applied the classical "onion peeling" inversion method (Goldman & Saunders, 1979). The two-stage process begins with fitting the wavelength dependent optical depth between 240 nm and 330 nm at each tangent altitude using the following equation:

$$\tau_\lambda = (A \times \lambda) + B + F \times \sigma_\lambda^{O_3} \quad (3)$$ (see Fig. 3).

The linear part of the equation corrects accounts for the contribution from the aerosol opacity that is approximated as being linear (coefficients A and B) over this narrow wavelength range (e.g. Figure 6.22 of Wolff et al., 2017). The amplitude factor F at each tangent altitude over the LOS is retrieved using the non-linear least square fitting algorithm, the Levenberg-Marquardt (Markwardt, 2009), by minimizing the residuals between the observed spectrum and the computed one from equation 3. After removing the aerosol contribution $[(A \times \lambda) + B\ ]$ the opacity caused solely by ozone becomes:

$$\tau_{\lambda}^{O_3} = F \times \sigma_{\lambda}^{O_3}. \qquad (4)$$

with the quantity F representing the column abundance of ozone along the occultation line of sight. The uppermost layer in the retrieval process is set at the tangent altitude where the retrieved amplitude factor is negative (no ozone detected), and the lowest layer above the surface of Mars corresponds to the lowest altitude as defined by the upper boundary τ_{λ}.

The second stage of the retrieval process is to convert the retrieved line of sight abundance of ozone to a vertical profile for the number density (n_{O_3}) of ozone using the onion peeling method. We treat the number density of O_3 as constant within each layer, and is derived at the uppermost layer using the following equation (5): $n_{O_{3},0} = F_0/(2dx_0)$, where dx_0 is half the path length within the layer. The number density in the atmospheric layer (*i*) is then calculated using the following equation (6):

$$n_{O_{3},i} = \frac{(F_i/2) - \sum_{j=0}^{i-1}\left[n_{O_{3},j} \times dx_j\right]}{dx_i}$$

Where dx_i is half the path length along the LOS in atmospheric layer (*i*). The bottom layer (*i=N*) is defined as the aforementioned lowest altitude. The retrieved vertical abundance profile for O_3 from solar occultation observation 20180503_012553_1p0b_UVIS_E is shown in Figure 3 (right panel). The retrieval process yielded ~154,000 successful retrievals from individual spectra, forming 4060 vertical profiles for a full Mars year.

3.2 Error analysis

The performance of the solar occultation channel UVIS was characterized by Vandaele et al. (2015) at several radiance scenarios in order to understand the sources of uncertainties in the UVIS spectra. The signal-to-noise ratio (SNR) followed closely the radiance that is limited by the attenuation from the atmosphere.

The uncertainties in the retrieved number densities of O_3 related to the instrumental noise are computed by propagating the error in the same fashion we applied the onion peeling method in section 3.1. After specifying the upper most layer in the retrieval, the error on the number density of ozone ($\delta n_{O_{3},0}$) is calculated in the following equation (7):

$$\delta n_{O_{3},0} = |\delta F_0|/(2dx_0)$$

where δF_0 is the 1σ statistical error on the fitted parameter F_0 that is computed from the covariance matrix during the Levenberg-Marquardt fitting mechanism. The error on the number density in the following (lower) layers (i=1→N) in the atmosphere ($\delta n_{O_3,i}$) is computed by propagating the errors in the following equation (8):

$$\delta n_{O_3,i} = \sqrt{\left[\frac{\left(\delta F_i^{\,2}/2^2\right) + \sum_{j=0}^{i-1}\left[\delta n_{O_3,j}^{\;\;2} \times dx_j^{\,2}\right]}{dx_i^{\,2}}\right]}$$

Where δF_i is the error on the retrieved parameter from the opacity spectrum at level (i) in the atmosphere, and $\delta n_{O_3,j}$ is the error on the ozone number density from the previous (upper) layers. Equation (8) indicates that the error in the retrieved number density $\delta n_{O_3,i}$ is a combination between the instrumental noise in the measured spectra at each tangent altitude and the quadratic sum of the errors on the previously computed ozone number density from the previous (upper) layers with corresponding half path length dx_j.

4. GEM-Mars model description

The expected behavior of ozone in the martian atmosphere can be simulated in General Circulation Models (GCM) with additional routines for photochemical calculations (Lefèvre et al., 2004; Daerden et al., 2019). For the comparison of our O_3 retrievals, we use the GEM-Mars GCM (Neary and Daerden, 2018; Daerden et al., 2019).

GEM-Mars is operated on a grid with a horizontal resolution of 4° × 4° and with 103 vertical levels reaching from the surface to ~ 150 km. It calculates atmospheric heating and cooling rates by solar and infrared radiation through atmospheric CO_2, dust and ice particles, and solves the primitive equations of atmospheric dynamics, using a time step of 30 s. The model simulates the evolution of dust, water vapor and water ice, CO_2 and CO_2 ice, and tracers for chemical composition. The chemistry routines in GEM-Mars calculate the photochemistry and gas-phase interactions of CO_2, H_2O and their photochemical products, including O_3 (Daerden et al., 2019). Comparisons of total ozone columns to observations of MARCI were presented in Daerden et al. (2019) and showed a good correspondence throughout most of the martian year and across most latitudes. Deviations from the MARCI observations were attributed to imperfections in the simulation of the water cycle. GEM-Mars currently uses bulk condensation of water vapor onto monodisperse ice particles of predescribed radius. While this simple treatment results in a reasonable simulation of the water cycle when compared to e.g. Mars Reconnaissance Orbiter (MRO) Compact Reconnaissance and Imaging Spectrometer for Mars (CRISM) observations (Smith et al., 2018; Daerden et al., 2019), it may explain the deviations that still exist, although models with more sophisticated schemes show more or less similar biases (e.g. Navarro et al., 2014; Shaposhnikov et al., 2018).

The NOMAD UVIS O_3 solar occultation dataset now allows for a first detailed evaluation of the simulated vertical distribution of O_3 in the model. In this paper we use a GEM-Mars simulation for generic conditions as presented in Daerden et al. (2019), with a self-consistently calculated dust distribution for an average non-global dust storm year. This has to be taken into account in the comparisons, as during the first year of NOMAD's science operations, a global dust storm occurred.

5. Results and discussion

5.1 Vertical O_3 profiles over polar latitudes

The most recognizable trend pertaining to the seasonal distribution of ozone is that the highest abundances are observed over the winter poles (e.g., Barth and Hord, 1971; Perrier et al., 2006; Clancy et al., 2016; Willame et al., 2018). Figure 4 shows the ozone vertical profiles as retrieved from ~27,000 spectra at selected seasonal bins over the north polar latitudes (60 °N – 88.7 °N). The seasonal bins are selected based on the frequency of the NOMAD coverage and to combine similarly behaving profiles in each bin. This provides a clear understanding of the seasonal evolution of the vertical profiles. The main "surface" layer of ozone on Mars is confined below 30 km, but as stated in section 1, our focus throughout this study is the characterization and evolution of high-altitude peaks of ozone that form above 30 km.

In the upper left corner of Figure 4 (L_s = 0 - 25°), we detect a high-altitude peak of ozone that is clearly visible in the altitude range 42 - 63 km, reaching its maximum intensity around 50 km, with abundance values ranging between n_{O_3}= 2×10^7 and 1×10^8 molecules/cm^3. As time progresses, the peak persists in its shape and altitude throughout early northern spring in the L_s= 0° - 25° range. After L_s= 25°, we notice changes in the shape of the vertical profile where ozone densities around 40 km have increased, weakening the inflection in the profile that existed at that altitude, filling the minimum in ozone between the high-altitude peak of ozone and the surface layer. The high-altitude peak maintains high concentrations of ozone, but the average enhancement (× 2) of ozone density at around 35 km lowers the contrast between the ozone abundances at 35 km and 50 km. After L_s= 45°, the high-altitude peak completely disappears, and the ozone density gradually decreases with height from 30 km to 70 km. In mid northern summer, a high-altitude but weaker peak re-emerges around 55 km, with ozone densities in the 8×10^6 - 4×10^7 molecules/cm^3 range, and this persists between L_s= 120° and 210°. The peak disappears again in early northern fall to mid northern winter (L_s= 210° - 330°), with lower values of ozone throughout the entire vertical range. The high-altitude peak re-emerges at the end of northern winter (L_s= 330° - 360°), with increasing densities at the peak between 10^7 and 10^8 molecules/cm^3 at around 45 km in altitude. It persists for at least 45 % of the martian year.

The vertical profiles from ~33,000 retrievals over the south polar latitudes (60 °S – 83.4 °S) are shown in Figure 5. In the upper left corner, a high-altitude ozone peak appears at 45 km between L_s= 0° and 25°, simultaneously with the high-altitude peak of the northern polar latitudes, showing similar densities between 2×10^7 and 2×10^8 molecules/cm^3. This high-altitude peak persists in location and intensity and location until L_s= 45°. Unlike its counterpart in the north, this high-altitude peak does not dissipate after L_s= 45°, but maintains high ozone densities over the 35

– 60 km altitude range between mid-southern fall and winter until L_s= 120°. The high-altitude peak completely disappears throughout southern spring until mid-southern summer (L_s= 330°). A newly formed high-altitude peak at the end of southern summer shows up at 60 km, with low ozone densities in the 3×10^6 - 2×10^7 molecules/cm^3 range, before gaining intensity at the beginning of the martian year. The high-altitude peak in the south polar latitudes is more defined in season, and it is present for more than 60 % of the year, showing similarities in location with its counterpart in the north during the first half of southern fall.

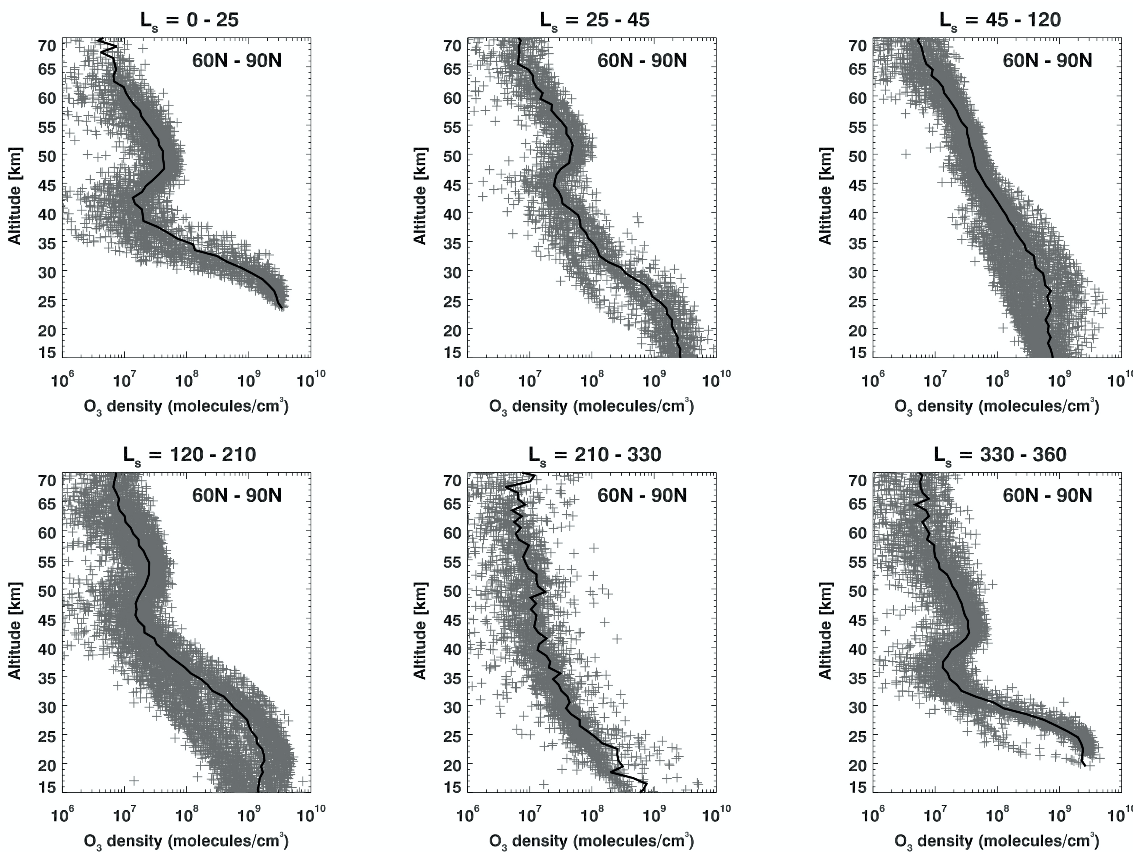

Figure 4. Vertical profiles of ozone as retrieved from ~27,000 spectra over the north polar latitudes (60 °N – 88.7 °N). This figure tracks the evolution of the vertical profile throughout an entire martian year at several seasonal bins. The gray dots represent the ozone density (molecules/cm^3) as retrieved from each transmittance spectrum at the relevant tangent altitude (km). The black curve represents the average profile between 15 and 70 km altitude. The upper left, middle and right panels represent the vertical ozone profiles during the sub-seasonal bin L_s= 0 - 25°, L_s= 25 - 45°, and L_s= 45 - 120°, respectively. The lower left, middle and right panels represent the vertical ozone profiles during the sub-seasonal bin L_s= 120 – 210°, L_s= 210 - 330°, and L_s= 330 – 360°, respectively. A high-altitude peak of ozone is detected over the north polar latitudes.

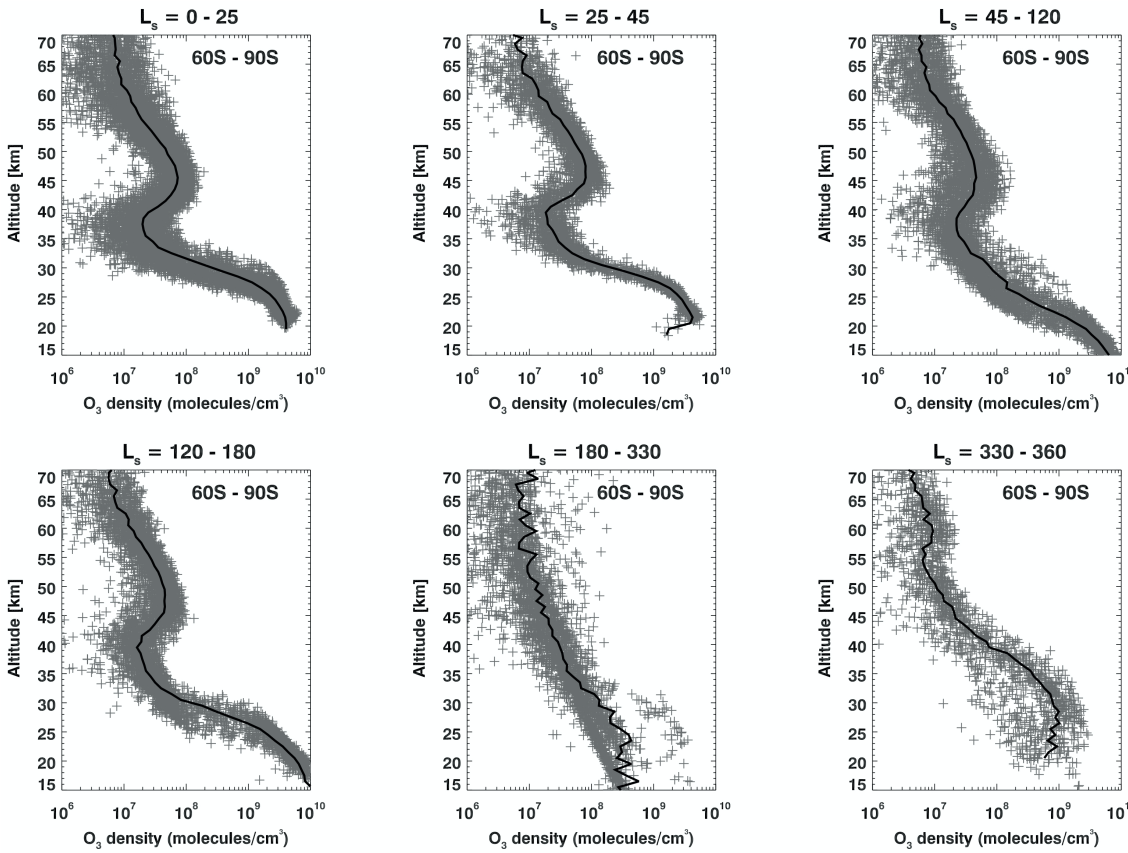

Figure 5. Vertical profiles of ozone as retrieved from ~33,000 retrievals over the south polar latitudes (60 °S – 83.4 °S). This figure tracks the evolution of the vertical profile throughout an entire martian year at several seasonal bins. The gray dots represent the ozone density (molecules/cm^3) as retrieved from each transmittance spectrum at the relevant tangent altitude (km). The black curve represents the average profile between 15 and 70 km altitude. The upper left, middle and right panels represent the vertical ozone profiles during the sub-seasonal bin L_s= 0 - 25°, L_s= 25 - 45°, and L_s= 45 - 120°, respectively. The lower left, middle and right panels represent the vertical ozone profiles during the sub-seasonal bin L_s= 120 – 280°, L_s= 180 - 330°, and L_s= 330 – 360°, respectively. A strong high-altitude peak of ozone is detected over the south polar latitudes.

5.2 Latitudinal evolution of the high-altitude O_3 peak in seasonal bands

Figure 6 shows the latitudinal distribution of the retrieved vertical O_3 abundance during four seasonal bands. The upper left plot shows this distribution around the beginning of northern spring at L_s= 0 ± 20°. The high-altitude peak of O_3 is prominent in the northern hemisphere between latitudes 60 °N and ~85 °N, reaching densities on the order of 10^8 molecules/cm^3 between altitudes 40 and 55 km, and has a counterpart in the southern hemisphere between latitudes 50 °S and ~85 °S, with similar ozone densities between 40 and 55 km altitude. In the north, the minimum in O_3 between the high-altitude peak and the one near the surface shows abundances < 10^7 molecules/cm^3, showing a complete separation between the two, with an order of magnitude lower densities in the high-altitude peak compared to the surface one, whereas in the south this minimum between the two is filled between latitudes 70 °S and 80 °S. The high-altitude peaks disappear at mid-latitudes in the south between 40 °S and 50 °S and in the north around 55 °N. The minimum in ozone abundances sets the boundaries between the high-altitude peaks at polar latitudes and an enhancement of ozone extending between the south (40 °S) and north (55 °N) of Mars. An enhancement in ozone abundance (~ 2×10^7 molecules/cm^3) connects the lower atmosphere and altitudes up to 65 km between 0 °N and 40 °N.

At the beginning of northern summer at L_s= 90 ± 20° (Fig. 6, upper right panel), the polar latitudes are not covered by UVIS, but a low-altitude enhancement of ozone is observed in the 25 – 35 km altitude range with densities at the 10^9 molecules/cm^3 level. No major high-altitude enhancement in ozone is observed within the UVIS coverage in the northern hemisphere below latitude 60 °N.

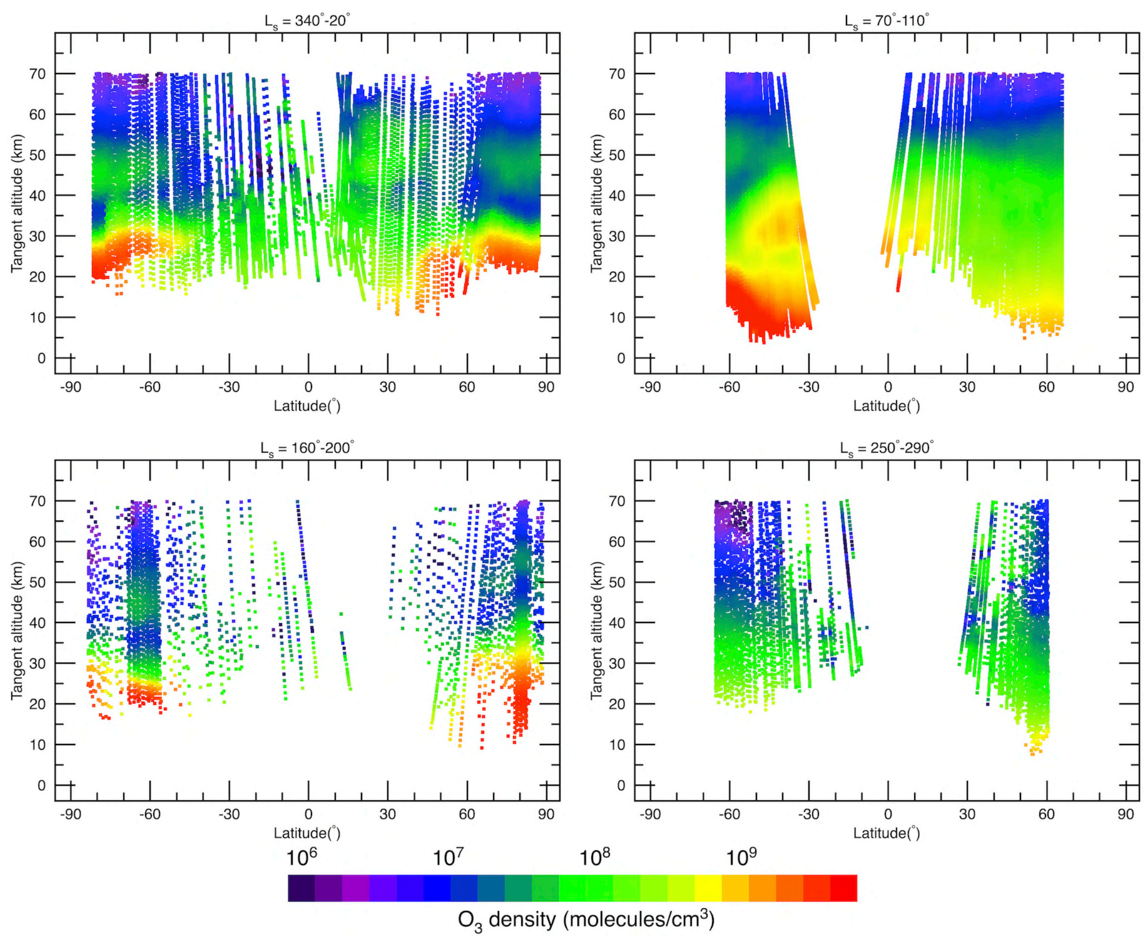

Figure 6. Latitudinal distribution (90 °S to 90 °N) of the retrieved vertical O_3 density (molecules/cm^3) below 70 km altitude at 4 sub-seasonal bands. The results are shown after applying a two-dimensional convolution of Δlatitude = 5° in the latitudinal dimension (x axis) and Δz = 3 km in the altitude dimension (y axis). The upper left panel shows the vertical distribution of ozone at the beginning of northern spring in the L_s range 340 - 20°. The upper right panel shows the vertical distribution of ozone at the beginning of northern summer in the L_s range 70 - 110°. The lower left panel shows the vertical distribution of ozone at the beginning of southern spring in the L_s range 160 – 200°. The lower right panel shows the vertical distribution of ozone at the beginning of southern summer in the L_s range 250 - 290°.

The high-altitude peaks of ozone show up again at high latitudes around southern spring at L_s= 180 ± 20° (Fig. 6, lower left panel). The peak in the south shows up between 55 °S and 70 °S in the altitude range 40 – 50 km, with ozone densities of 6-8 ×10^7 molecules/cm^3, but does not persist between 70 °S and 85 °S. In contrast, the high-altitude peak of ozone in the north persists between 60 °N and 85 °N, and is located in the altitude ranges 45 - 55 km, 55 - 60 km, and 45 - 55 km, at latitudes ranges 60 °N - 75 °N, 75 °N - 85 °N, and > 85 °N, respectively, with ozone densities in the upper 10^7 molecules/cm^3.

The polar latitudes were not covered by UVIS in the southern summer at L_s= 270 ± 20° (Fig. 6, lower right panel). In the covered latitudinal range, no distinct high-altitude peaks of ozone were observed, but an enhancement in ozone abundance (~ 10^8 molecules/cm^3) is observed at high altitudes below 70 km in latitude range 30 °S – 55 °N.

5.3 Seasonal evolution of the high-altitude O_3 peak in latitude bands

The seasonal distribution of the vertical abundance of ozone is shown in Figure 7. In the high latitude range 60 °N – 70 °N, the high-altitude peak of ozone is well observed during northern spring until L_s= 40°, with densities above 10^8 molecules/cm^3.

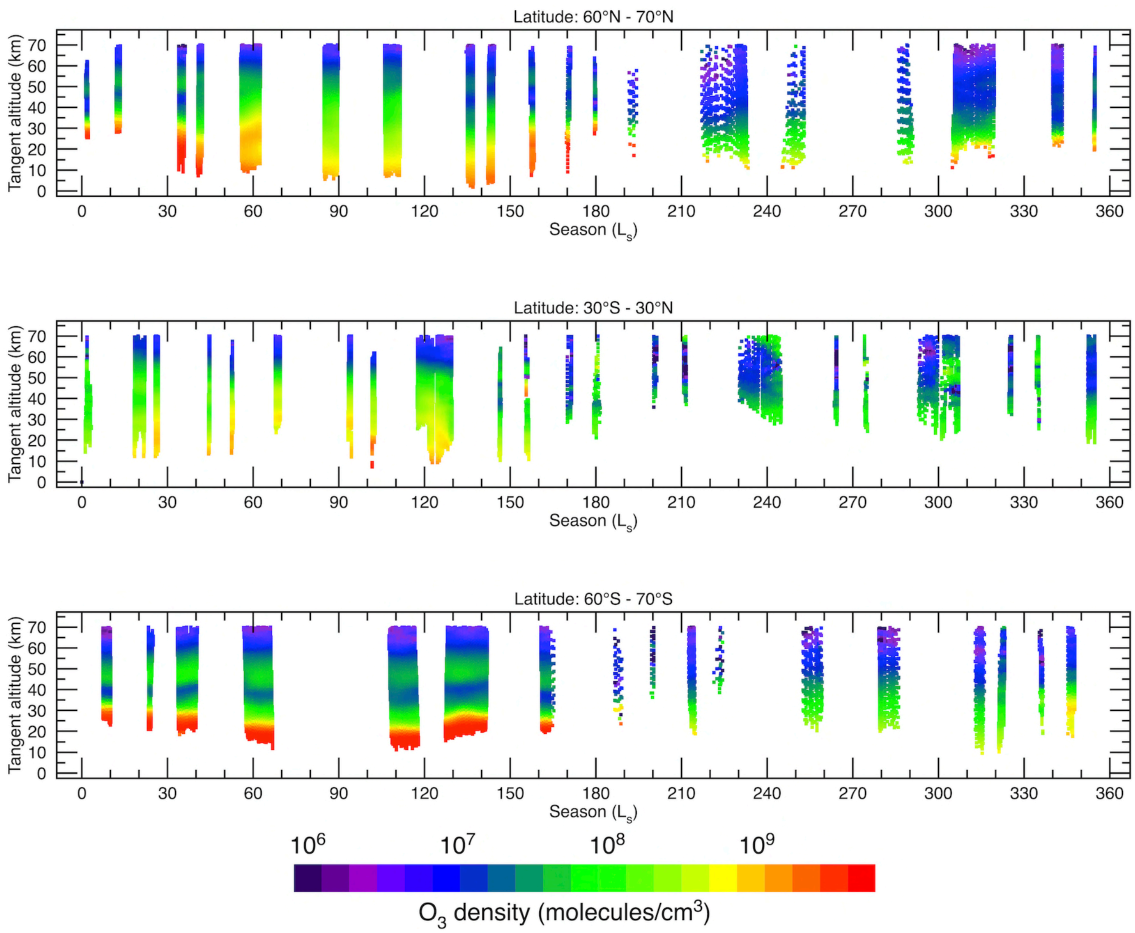

Figure 7. Seasonal distribution (L_s = 0 - 360°) of the retrieved vertical O_3 density (molecules/cm^3) below 70 km altitude at 3 latitude bands. The results are shown after applying a two-dimensional convolution of ΔL_s = 5° in the seasonal dimension (x axis) and Δz = 3 km in the altitude dimension (y axis). The upper panel represents the vertical distribution of ozone at different the local time coverage at high northern latitudes between 60 °N and 70 °N. The middle panel represents the vertical distribution of ozone over a larger latitude band over the equator (30 °S to 30 °N) due to the low frequency of UVIS observations around the equator. The lower panel represents the vertical distribution of ozone at high southern latitudes between 60 °N and 70 °N where a strong high-altitude peak of ozone is observed.

The enhancement of ozone around 40 km altitude fills the minimum in ozone between the high-altitude peak and the main ozone layer near the surface of Mars, making the high-altitude peak disappear between mid-northern spring (L_s > 40°) until mid-northern summer at ~ L_s = 130°. The high-altitude peak re-merges and lasts until the beginning of southern spring, but it is limited in its vertical extent (< 10 km) and intensity, with densities < 10^7 molecules/cm^3. Throughout the rest of the martian year, the ozone is depleted at the altitudes of the high-altitude peak, before the re-appearance of the peak right before the end of northern winter at L_s = 355°.

Due to the less frequent UVIS coverage of the equatorial regions, we combined the ozone distribution between 30 °S and 30 °N (Fig. 7, middle panel). There is no major presence of the high-altitude peak of ozone in around the equator throughout the entire martian year. In contrast, a very well defined high-altitude peak of ozone is present over high-southern latitudes between 60 °S and 70 °S (Fig. 7, lower panel), with maximum densities surpassing 10^8 molecules/cm^3 in southern fall, and it remains throughout southern fall and winter, before completely disappearing for the rest of the martian year.

5.4 The high-altitude O_3 peak during sunrise/sunset occultations

The coverage of the UVIS solar occultation observations provides a window into the evolution of the vertical distribution of ozone and yields important information on the efficiency of the photochemical production/destruction of high-altitude ozone (e.g., Lefèvre at al., 2004; Montmessin & Lefèvre, 2013; Daerden et al., 2019).

By definition, the geometry of a solar occultation only allows observations at locations transitioning between daylight and night. Most of the time, these solar occultations are at either local sunrise or at sunset. Observations at sunrise observe the part of the atmosphere that has just emerged into sunlight after being in darkness during the night, while observations at sunset observe atmosphere that has been in sunlight all day. At polar latitudes the observations can also sample the transition between areas in polar night and daylight, or between areas with 24 hour daylight and night. In the figures described below, we plot retrieved ozone profiles as a function of local time to separate the cases of sunrise, sunset, and polar observations. However, there is no implied difference between observations at local times of 6:00 and 8:00 (for example), both are sunrise occultations.

Figure 8 shows the vertical profile of ozone over the north polar latitudes during four seasons on Mars. During northern spring (Fig. 8, upper left panel), the north polar region is illuminated, and the high-altitude peak of ozone between 45 and 60 km altitude persists and maintains abundances > 10^8 molecules/cm^3. During northern summer (Fig. 8, upper right panel), the high-altitude peak of ozone is located between 50 and 60 km altitude, but with low abundances (6-8 $\times 10^7$ molecules/cm^3) compared to northern spring. The peak remains a distinct entity from the near surface enhancement of ozone. At southern spring and summer seasons (Fig. 8, lower left and right panels) when the north polar region is no longer illuminated by the sun, the high-altitude peak of ozone is observed between 40 and 55 km altitude with ozone abundances not exceeding 10^8 molecules/cm^3.

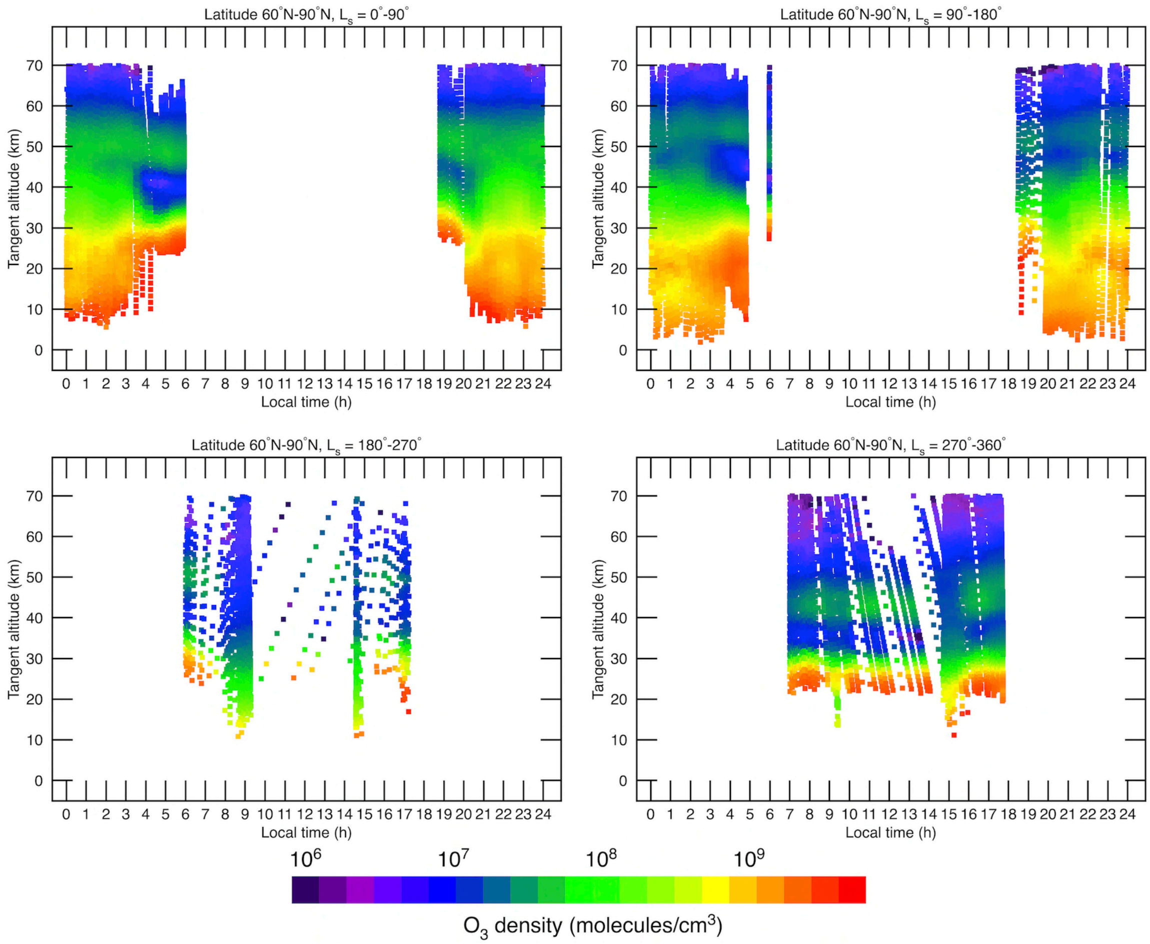

Figure 8. Vertical distribution of the retrieved O_3 abundance (molecules/cm^3) below 70 km altitude at 4 seasons on Mars using sunrise and sunset occultations, over the north polar latitudes (60 °N – 90 °N). The results are shown after applying a two-dimensional convolution of ΔLT= 1 h in the local time dimension (x axis) and $\Delta z = 3$ km in the altitude dimension (y axis). The upper left and right panels represent the local time distribution of ozone during northern spring and summer seasons, respectively. The lower left and right panels represent the local time distribution of ozone during southern spring and summer seasons, respectively. The high-altitude peak of ozone is still observed during daytime.

Over the south polar latitudes, the high-altitude peak of ozone persists during southern fall (Fig. 9, upper left panel). The vertical location is maintained between 40 and 60 km altitude, as well as the abundance (~ 5 $\times 10^8$ molecules/cm^3). The same pattern is observed around southern winter (Fig. 9, upper right panel), but with lower abundances of ozone in the high-altitude peak (<

10^8 molecules/cm^3). The sunrise and sunset occultations both show the high-altitude peak of ozone, indicating that the peak could persist throughout the day. The high-altitude peak of ozone completely disappears during southern spring and winter (Fig. 9, lower panels) when the south polar regions are illuminated by the sun, showing a minimum in ozone in the altitude range 40 – 60 km of the previously existing peak. Most of the atmospheric ozone is confined below 40 km altitude, higher than the 30 km altitude in the previous seasons.

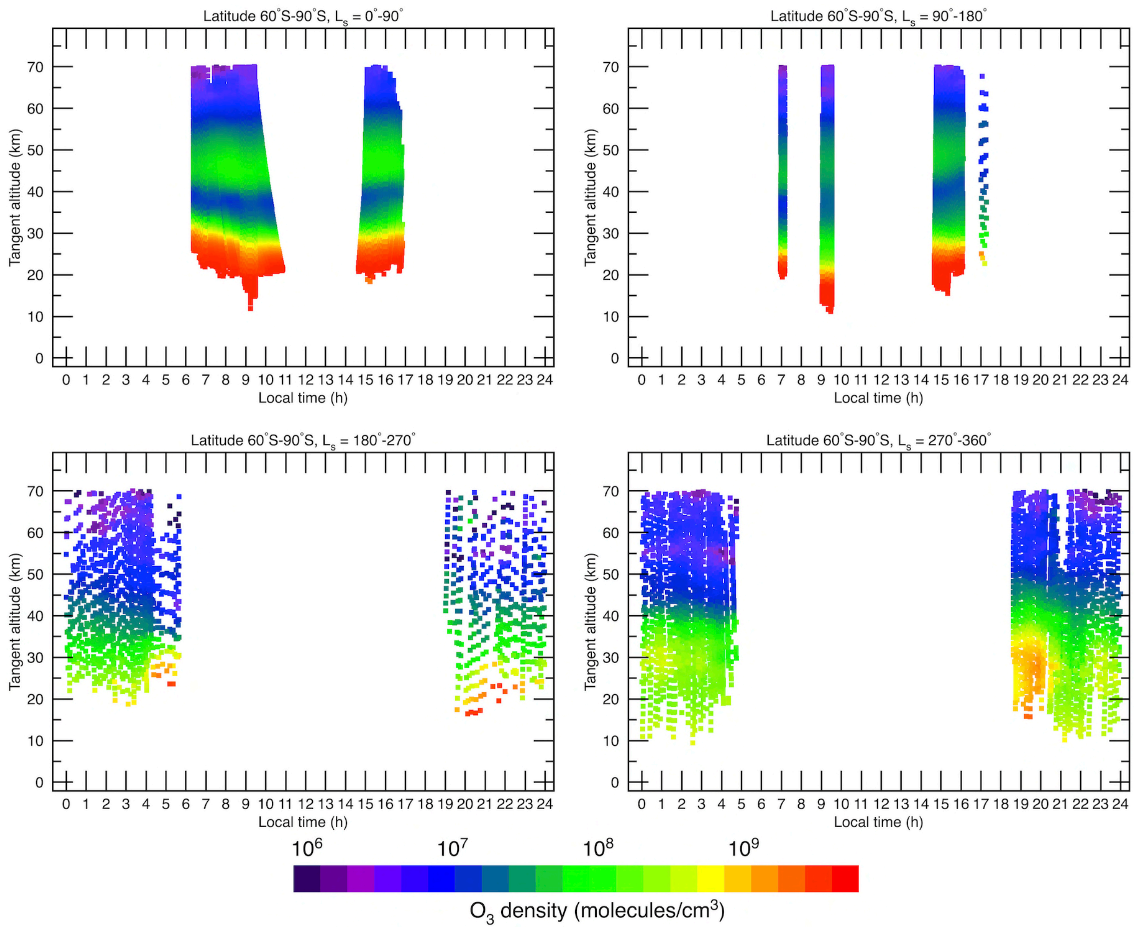

Figure 9. Vertical distribution of the retrieved O_3 abundance (molecules/cm^3) below 70 km altitude at 4 seasons on Mars, over the south polar latitudes (60 °S – 90 °S) using sunrise and sunset occultations. The results are shown after applying a two-dimensional convolution of ΔLT= 1 h in the local time dimension (x axis) and $\Delta z = 3$ km in the altitude dimension (y axis). The upper left and right panels represent the local time distribution of ozone during southern fall and winter seasons, respectively. The lower left and right panels represent the local time distribution of ozone during southern spring and summer seasons, respectively. The high-altitude peak of ozone is prominently observed during the southern fall and winter seasons.

Figure 10 shows the vertical distribution of ozone from sunrise and sunset occultations in the mid-latitude range (30 °N – 60 °N). The high-altitude peak of ozone is almost non-existent, and the ozone abundances show an increase at high altitudes due to the decrease in the hygropause altitude at this time of the year (Clancy & Nair, 1996).

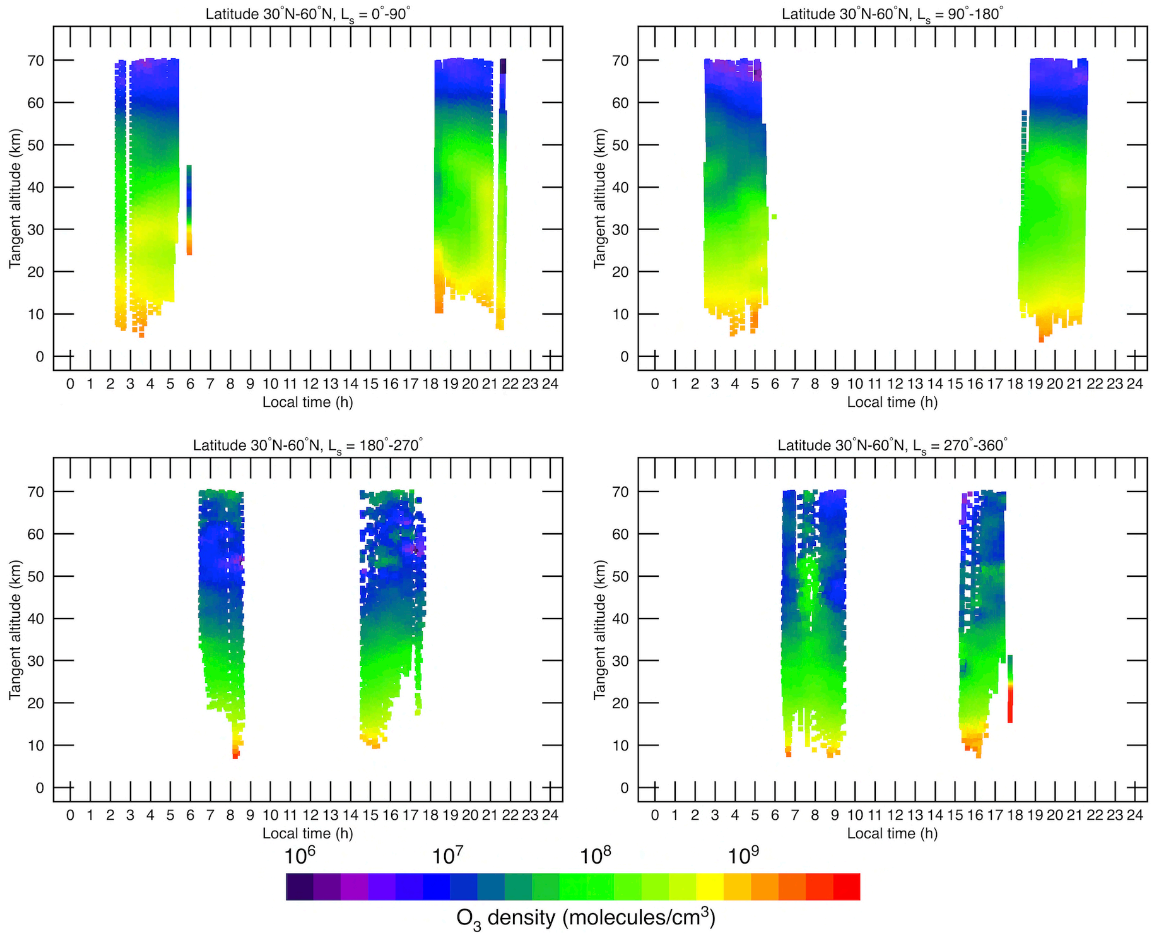

Figure 10. Vertical distribution of the retrieved O_3 abundance (molecules/cm^3) below 70 km altitude at 4 seasons on Mars, over the mid-latitudes in the north (30 °N – 60 °N) using sunrise and sunset occultations. The results are shown after applying a two-dimensional convolution of ΔLT= 1 h in the local time dimension (x axis) and Δz = 3 km in the altitude dimension (y axis). The upper left and right panels represent the local time distribution of ozone during northern spring and summer seasons, respectively. The lower left and right panels represent the local time distribution of ozone during southern spring and summer seasons, respectively. There is no clear presence of the high-altitude peak of ozone.

During northern spring around mid-latitudes in the south (30 °S – 60 °S), the high-altitude peak of ozone is still observed (Fig. 11, upper left panel), but with low ozone abundances (< 10^8 molecules/cm^3), contrary to its counterpart in the north that is almost non-existent around this season. More ozone around 40 km is present in the sunset occultations, filling the minimum in ozone between the surface layer of zone and the high-altitude peak. The peak persists during southern winter (Fig. 11, upper right panel), but it becomes weak during sunrise occultations. During southern spring and summer seasons, the high-altitude peak shows no appearance in the solar occultations.

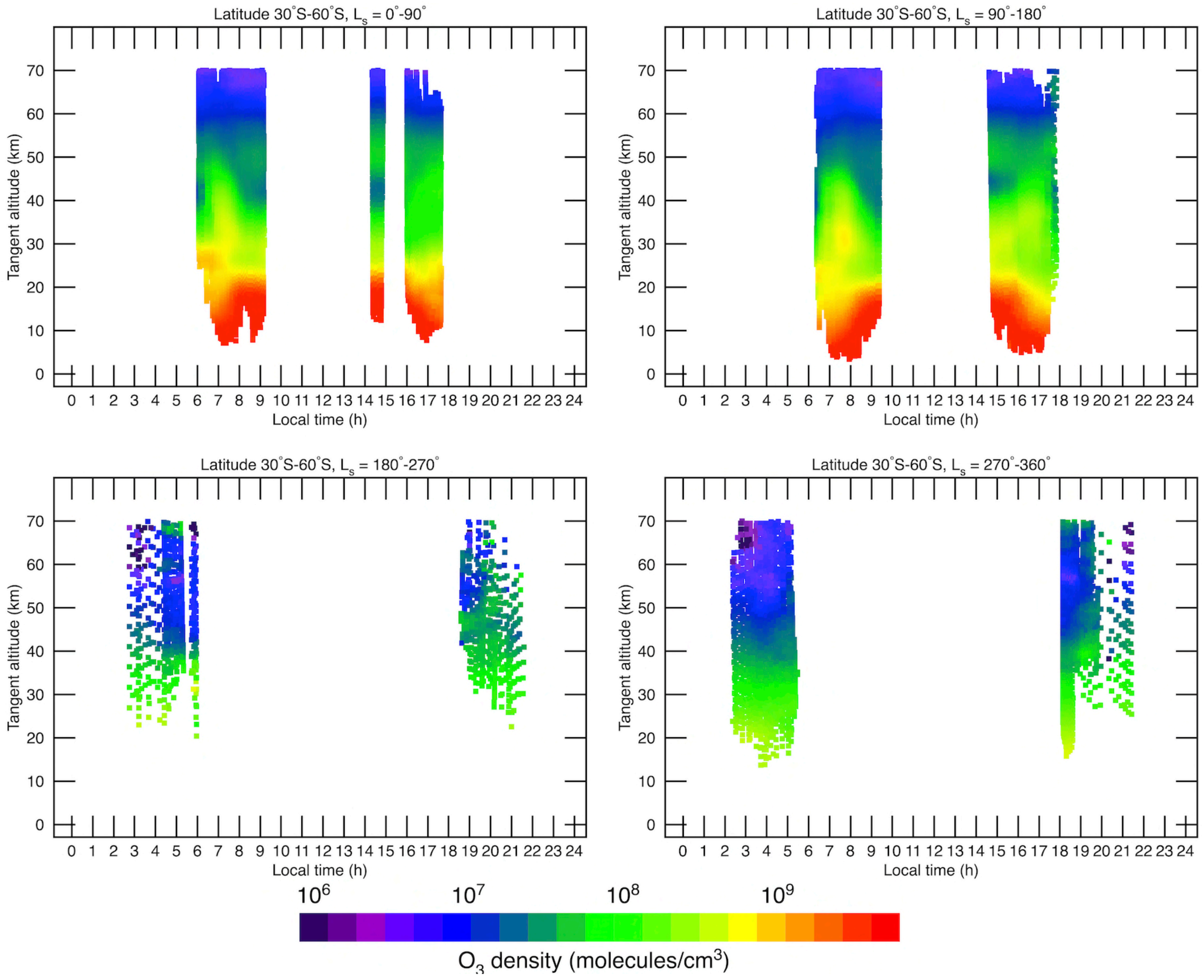

Figure 11. Vertical distribution of the retrieved O_3 abundance (molecules/cm^3) below 70 km altitude at 4 seasons on Mars, over the mid-latitudes in the south (30 °S – 60 °S) using sunrise and sunset occultations. The results are shown after applying a two-dimensional convolution of ΔLT= 1 h in the local time dimension (x axis) and $\Delta z = 3$ km in the altitude dimension (y axis). The upper left and right panels represent the local time distribution of ozone during southern fall and winter seasons, respectively. The lower left and right panels represent the local time distribution of ozone during southern spring and summer seasons, respectively. There is no clear presence of the high-altitude peak of ozone during southern spring and summer seasons.

Due to the scarcity of observations around equatorial latitudes, the ozone distribution presented in Figure 12 shows results for latitudes between 30 °S and 30 °N. The high-altitude peak of ozone no longer exists independently at equatorial latitudes. During southern spring and summer (Fig. 12, lower panels), the ozone becomes depleted above 40 km in the sunset occultations.

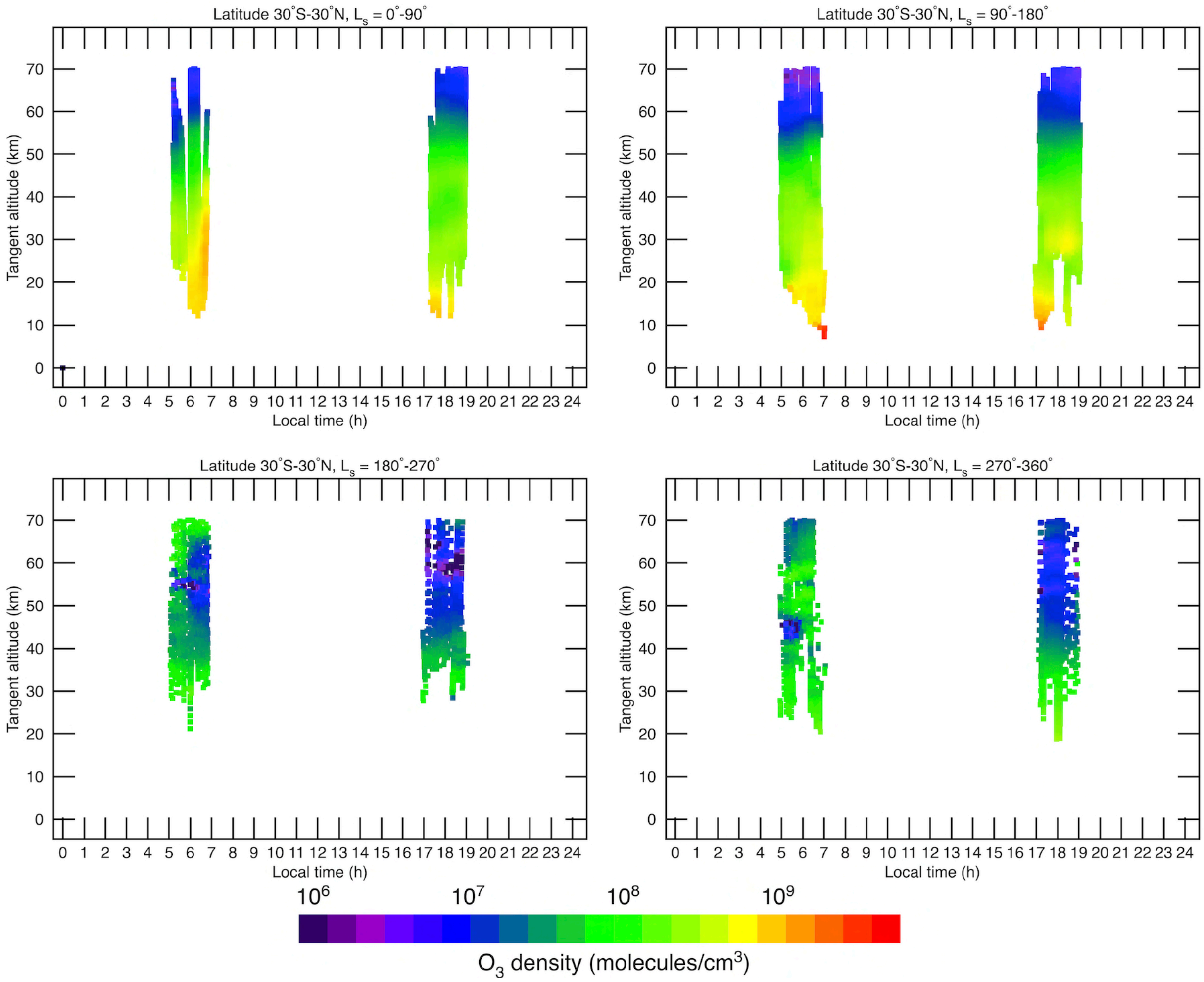

Figure 12. Vertical distribution of the retrieved O_3 abundance (molecules/cm^3) below 70 km altitude at 4 seasons on Mars, over the equatorial latitudes (30 °S – 30 °N) using sunrise and sunset occultations. The results are shown after applying a two-dimensional convolution of ΔLT= 1 h in the local time dimension (x axis) and Δz = 3 km in the altitude dimension (y axis). The upper left and right panels represent the local time distribution of ozone during northern spring and summer seasons, respectively. The lower left and right panels represent the local time distribution of ozone during southern spring and summer seasons, respectively. There is no clear presence of the high-altitude peak of ozone.

5.5 Evolution of the high-altitude O_3 peak on the hemispheric scale

The most complete picture of the vertical distribution of ozone over a full Mars year is presented in Figure 13, where its seasonal evolution is shown in both hemispheres. The high-altitude peak in the northern hemisphere pertaining to latitudes > 50 °N is present until L_s = 40° (Fig. 13, upper panel). Later in the season the produced ozone from below 45 km altitude fills the minimum in ozone between the high-altitude layer and the surface layer until mid-northern summer at L_s = 130°. The high-altitude peak of ozone re-emerges again as a distinct layer until the end of northern summer. The peak over high latitudes completely disappears throughout northern fall and most of winter before forming again at L_s = 340°.

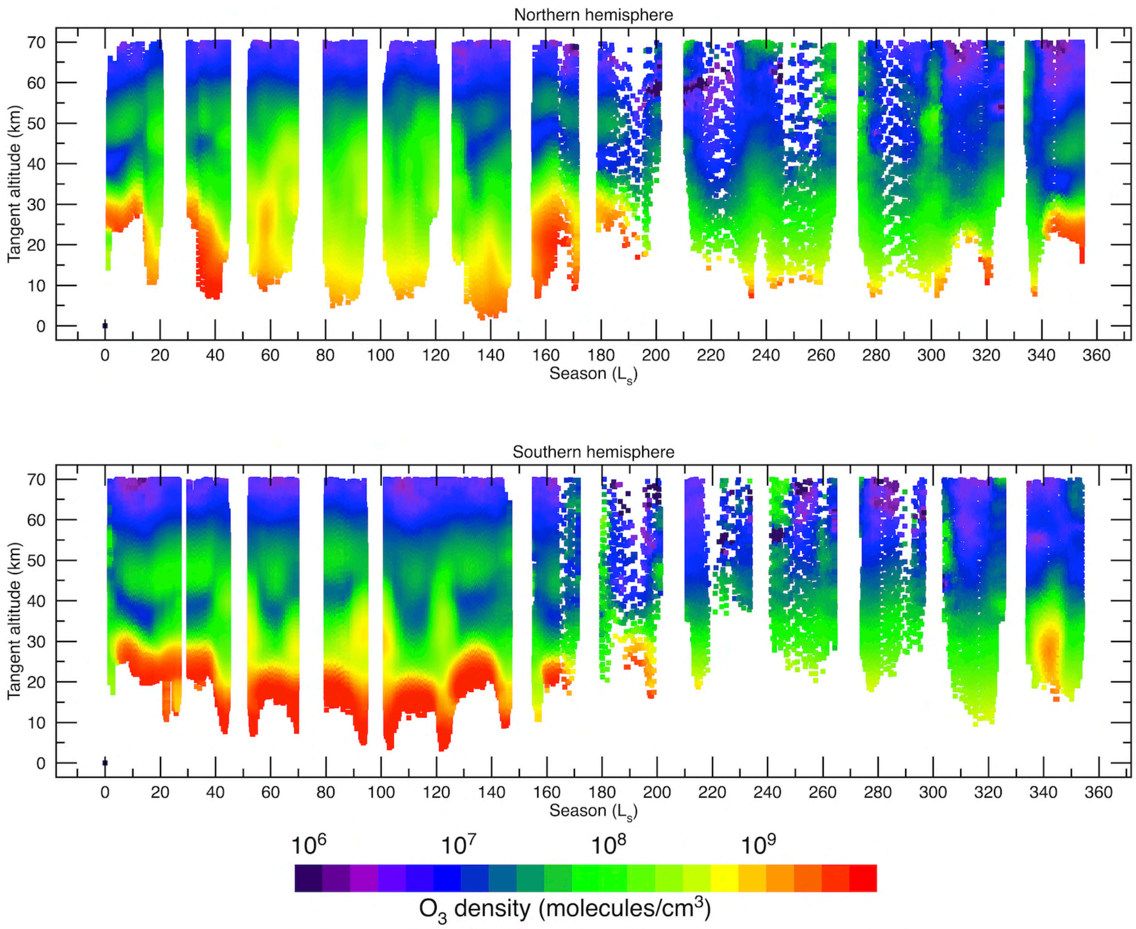

Figure 13. Seasonal distribution of the retrieved vertical O_3 abundance (molecules/cm^3) in the northern (upper panel) and southern (lower panel) hemispheres. The results are shown after applying a two-dimensional convolution of $\Delta L_s = 5$ ° in the local time dimension (x axis) and $\Delta z = 3$ km in the altitude dimension (y axis). The high-altitude peaks of ozone are visible in both hemispheres during northern spring (southern fall).

The high-altitude ozone peak is more prominent in the southern hemisphere (Fig. 13. Lower panel), and is mostly attributed to latitudes poleward of 60 °S. This layer maintains altitude and intensity throughout southern fall and winter seasons until $L_s = 170°$. The enhancement in the ozone abundance around $L_s = 50°$, 90° and 120° in the altitude range 30 – 40 km is mostly attributed to the low latitudes in the south. The high-altitude peak of ozone in the southern hemisphere completely disappears throughout the rest of the martian year, leaving the atmosphere depleted of ozone above 40 km altitude over the high latitudes in the southern hemisphere.

5.6 Comparisons with the GEM model results

The vertical distribution of ozone as a function of latitude in seasonal bands as modeled by GEM-Mars is shown in Figure 14. To allow a one-to-one comparison with the UVIS retrievals, the GEM-Mars O_3 abundance values are given at the same altitude, longitude, latitude, local time and L_s at each UVIS observation. During the beginning of northern spring (Fig. 14, upper left panel), the GEM-Mars results very well reproduce the general behavior of ozone in the atmosphere as observed by the UVIS retrievals, especially with the enhancement of ozone above 35 km. The main difference is that GEM predicts large amounts of ozone over the entire 35 and 55 km altitude range, with values in the $5 \times 10^7 - 2 \times 10^8$ molecules/cm^3 range at polar latitudes. In contrast, the values from UVIS retrievals show similar abundance values of a few times 10^8 molecules/cm^3 but over a smaller vertical range in the atmosphere between altitudes 40 and 53 km. This can be explained by deviations of the simulated water vapor profile (Aoki et al., 2019) mostly caused by the simple treatment of water ice clouds in GEM-Mars. In Aoki et al. (2019), Fig. 8c, it is shown that GEM-Mars underestimates the water vapor abundances at the locations of the high-altitude ozone peak, causing the model to form more ozone than observed.

Around the beginning of northern summer at $L_s = 90 \pm 20°$ (Fig. 14, upper right panel), the high ozone abundances below 40 km altitude over the mid-latitudes in the south are in good agreement with the UVIS retrievals. However, GEM-Mars predicts a distinct high-altitude peak of O_3 between 40 and 50 km, with a minimum in ozone between 20 and 40 km altitude over the mid-latitudes in the north, whereas UVIS retrievals show a continuous enhancement in the ozone abundances beginning at 60 km altitude and gradually decreasing with height. As was shown and discussed in Daerden et al. (2019), the current GEM model simulates higher water abundances than observed in the aphelion season because of the presence of the aphelion cloud belt and imperfectly simulated cloud radiative effects (e.g. Daerden et al., 2019, Figs. 15, 16 and 28). The excess in water vapor between L_s= 60 and 100° shown in Fig. 15 in Daerden et al. (2019) can be considered as the direct cause of the low ozone abundances shown in Fig. 14, upper right panel. Indeed the impact of water vapor abundances on ozone is very strong and immediate (Lefèvre et al., 2004; Daerden et al., 2019).

The extent and magnitude of the high-altitude enhancement of ozone at polar latitudes in the north and south are repeated in the GEM-Mars results around the beginning of southern spring at $L_s = 160 \pm 200°$ (Fig. 14, lower left panel). The general behavior of vertical ozone with the high-altitude peak is well reproduced, but the GEM results show average abundances around 10^8 molecules/cm^3, peaking in the 40 - 45 km altitude range whereas UVIS retrievals have lower abundance of around 5×10^7 molecules/cm^3, peaking around 50 and 55 km altitudes. The explanation is very similar to before, i.e. resulting from the low water abundances in GEM-Mars compared to NOMAD water observations (Aoki et al., 2019, Fig. 6a) at the location of the ozone peak.

Interestingly, the GEM-Mars results show depleted ozone abundance values over 25 km altitude around the beginning of southern summer at $L_s = 250 \pm 290$ ° (Fig. 14, lower right panel), and a slight enhancement in ozone between 45 and 55 km altitude around 60 °N. UVIS retrievals show an enhancement of ozone between 40 and 60 km over the mid-northern latitudes, with abundances > 10^8 molecules/cm^3. The simulated depletion is a result of excessive water vapor simulated in the 25-50 km altitude range at southern altitudes in this season (Aoki et al., 2019, Fig. 6e).

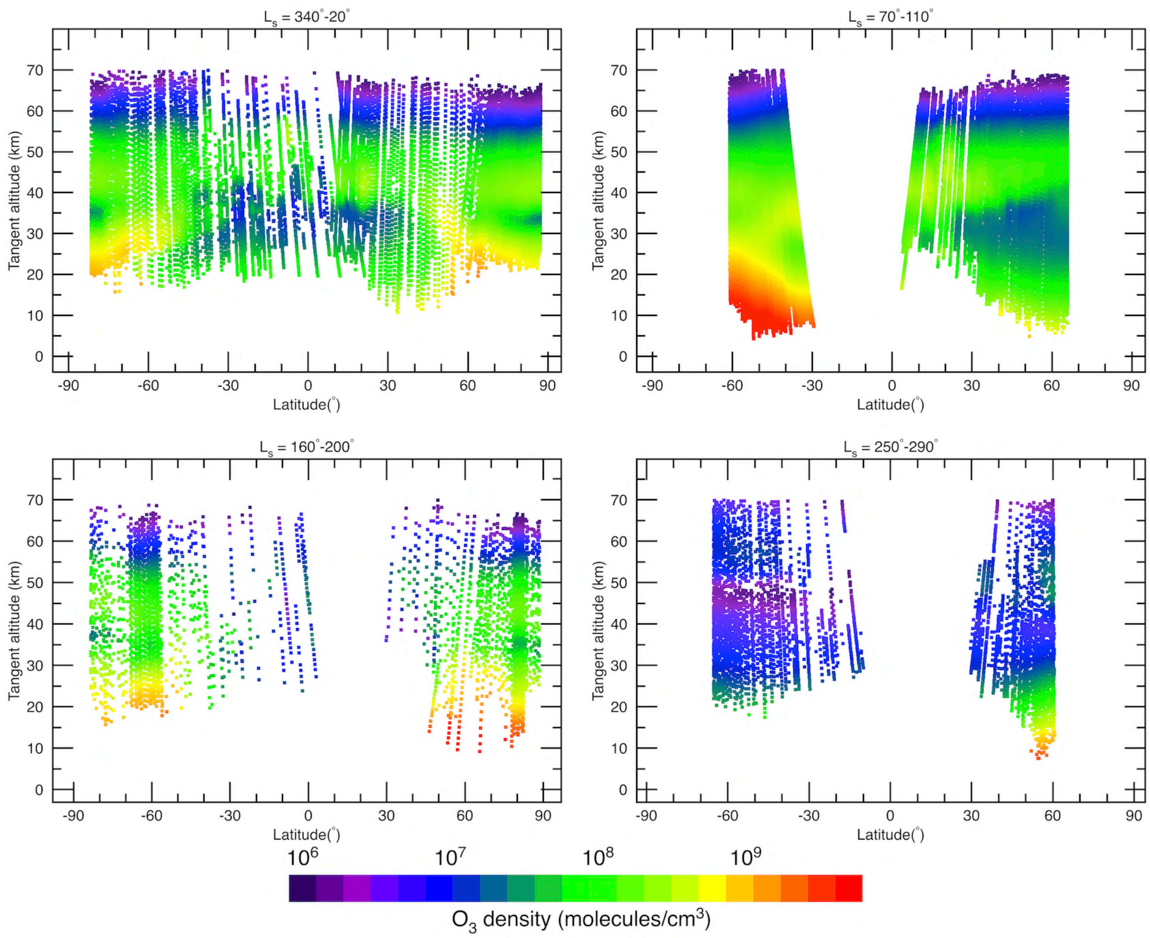

Figure 14. GEM-Mars model simulation of ozone vertical abundance averaged over the altitudes, latitudes, longitudes, L_s and local times observed by UVIS. The results are shown after applying the same two-dimensional convolution of Δlatitude = 5° in the latitudinal dimension (x axis) and Δz = 3 km in the altitude dimension (y axis) as the ones in Figure 6 where UVIS retrievals are shown. The upper left panel shows the GEM vertical distribution of ozone around the beginning of northern spring in the L_s range 340 - 20°. The upper right panel shows the GEM vertical distribution of ozone at the beginning of northern summer in the L_s range 70 - 110°. The lower left panel shows the GEM vertical distribution of ozone at the beginning of southern spring in the L_s range 160 – 200°. The lower right panel shows the GEM-Mars vertical distribution of ozone at the beginning of southern summer in the L_s range 250 - 290°.

The full seasonal distribution of the vertical abundance of ozone using GEM-Mars simulations in the northern and southern hemispheres is shown in Figure 15. In the northern hemisphere (upper panel), the high-altitude ozone peak is well described in the GEM-Mars simulations, especially during northern summer. The ozone enhancement above the minimum at 35 km altitude between L_s = 0 and 10°, as well as between 40 and 45 km altitude between L_s = 60 and 70°, both in abundance and location. The high-altitude abundances of ozone below 55 km are also well in agreement with the UVIS retrievals during northern summer, but a difference between GEM-Mars and UVIS retrievals is observed between 20 and 30 km altitude between L_s = 80 and 140°, showing a depletion in the O_3 abundances in the GEM-Mars results.

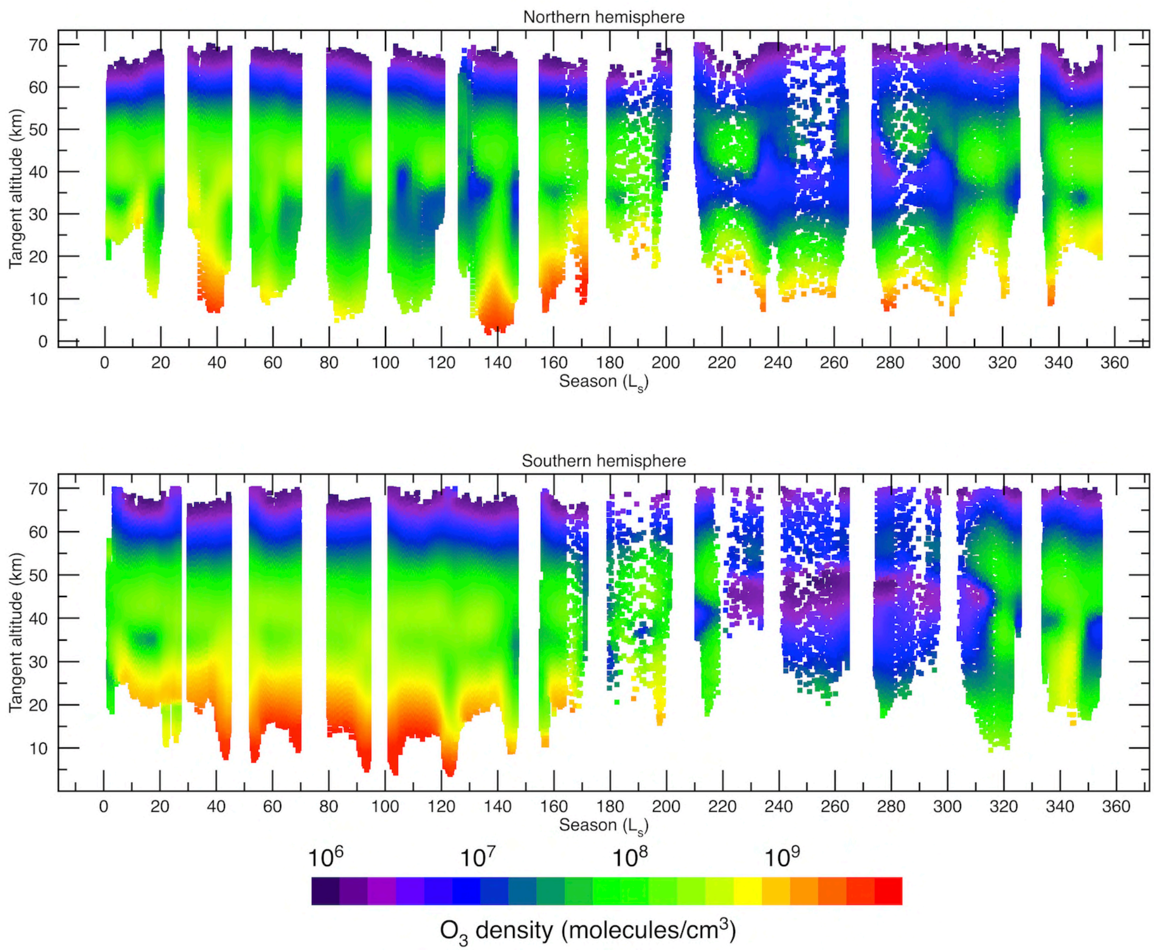

Figure 15. GEM-Mars model simulations of the seasonal distribution of the retrieved vertical O_3 abundance (molecules/cm^3) averaged over the altitudes, latitudes, longitudes, L_s and local times observed by UVIS in the northern (upper panel) and southern (lower panel) hemispheres. The results are shown after applying similar two-dimensional convolution of $\Delta L_s = 5$ ° in the local time dimension (x axis) and $\Delta z = 3$ km in the altitude dimension (y axis) as the ones in Figure 13 where UVIS retrievals are shown.

This readily results from issues with the simulation of water vapor abundances in the aphelion season, related to radiative effects of clouds in the aphelion cloud belt, as was extensively discussed in Daerden et al. (2019). The high-altitude peak between L_s = 160 and 170° is well reproduced by GEM-Mars, but it presents higher abundances peaking at 8 $\times 10^8$ molecules/cm^3, exceeding ~ 8 times the peak values by the UVIS retrievals. This is related to the low water vapor abundances simulated in GEM in the higher altitudes/high latitude regions, as shown in Daerden et al. (2019) and Aoki et al. (2019). The GEM-Mars simulations predict high-altitudes peaks in O_3 abundances around L_s = 220° and between L_s = 280° and 360° with various abundances and vertical extents. However, the UVIS retrievals did not detect similar isolated peaks, and that could be attributed to the effect of the global dust storm within that period of the martian year during the MY 34 (e.g., Guzewich et al., 2018; Smith et al., 2019). Dedicated simulations for the global dust storm were presented in Neary et al. (2020). The high-altitude peak seen by UVIS at L_s = 350° between the 40 and 50 km altitude is well produced by GEM-Mars, but with ~ 5 times higher O_3

abundances compared to UVIS, again as a result of the low water vapor abundances simulated at high altitude/high latitudes (Daerden et al., 2019; Aoki et al., 2019).

In the southern hemisphere (Fig. 15, lower panel), the key features in the high-altitude peak of ozone are well depicted in the GEM-Mars results, notably around L_s = 20°, 65° and 130°. In particular, the peak location in the altitude range 40 – 50 km throughout southern fall and winter is consistent with the UVIS retrievals. The high-altitude peak in the south polar latitudes is more prominent compared to its counterpart in the north and it persists for over two seasons on Mars, something that is well reproduced in the GEM-Mars simulations. However, the GEM-Mars results again predict higher ozone abundance in the high-altitude peak that are as much as 5 times larger than the retrieved abundances by UVIS. GEM predicts a high-altitude peak between L_s = 180 and 200° that is not observed with UVIS. In the southern summer at ~ L_s = 340°, an enhancement of ozone at about 20 km is observed in both the UVIS and the GEM-Mars results, but GEM-Mars produced a high-altitude peak between ~ L_s = 340 and 360° that is not found in the UVIS retrievals. As for the northern observations, the differences in the GEM-Mars simulations with the data can here also be attributed to biases in the simulated water vapor abundances, as shown and discussed before (Daerden et al., 2019; Aoki et al., 2019).

6. Discussion and summary

The stellar occultations by SPICAM (Lebonnois et al., 2006) provided nighttime vertical profiles of ozone between spring equinox and winter solstice. The observations, when combined with theoretical studies (Montmessin and Lefèvre, 2013) to cover polar regions, reported the presence of an elevated layer of ozone between 40 and 60 km in altitude in the southern polar night, repeatedly observed during three Mars years. This layer is predicted to appear essentially during the night when ozone is formed, before being rapidly photolyzed after sunrise (Montmessin et al., 2013; 2017). However, retrievals using UVIS solar occultations shown here have detected the strong presence of a high-altitude layer of ozone in the same altitude range (Figure 9, upper panels). UVIS shows a similar pattern in the ozone abundance and peak location in the sunrise and sunset occultations. Indeed, the high-altitude peak in the south polar region persisted throughout the entire southern fall and winter seasons, with a slight decrease in intensity during southern winter, before completely disappearing for the rest of the year and re-emerging at ~ L_s =330° (Fig. 5, lower right panel).

General circulations models (Montmessin et al., 2013) attribute the formation of the nocturnal layer to the large-scale transport of oxygen in the martian atmosphere from mid-latitude regions illuminated by solar flux to the polar regions where oxygen atoms recombine at night to form ozone in the high-altitude layer. SPICAM provided observations in the north polar region during northern autumn and winter (L_s = 180 - 360°) but could not identify a pronounced high-altitude layer, a conclusion shared by the GCM model for the north polar latitudes. As a result, Montmessin et al. (2013) concluded that the aforementioned large-scale transport of oxygen is less efficient in the north, and that the destruction of ozone through reactions with hydrogen radicals is ∼100 times stronger above the northern winter pole compared to its southern counterpart, ruling out the formation of a secondary layer of ozone in the north polar regions. However, the more complete coverage provided by UVIS indicates that the formation of a high-altitude ozone layer in the north polar regions does occur at the end of northern winter at L_s = 330° (Fig. 4, lower right panel, and Fig. 8, lower right panel), lasting until mid-northern spring at L_s = 45° (Fig. 4, upper left and middle panels, and Fig. 8, upper left panel), but its magnitude and seasonal extent are smaller compared to their counterparts in the south.

In summary, the UVIS spectrometer onboard TGO provided ~ 4100 solar occultation profiles of the atmosphere of Mars covering a full Mars year between MY 34 at L_s = 163° on April 21, 2018, and MY 35 on March 9, 2020. UVIS retrievals provide the most complete vertical O_3 mapping ever produced, describing the seasonal, spatial and local time distribution of ozone in detail.

UVIS retrievals reveal the presence of a high-altitude peak of ozone between 40 and 60 km in altitude over the north polar latitudes for over 45 % of the martian year, particularly during mid-northern spring, late northern summer-early southern spring, and late southern summer. UVIS also detected the presence of a second high-altitude peak in the south polar latitudes, lasting for over 60 % of the year including southern autumn and winter. The evolution of the high-altitude O_3 peak on the hemispheric scale shows that it is more prominent in the south and is mostly confined to latitudes poleward of 60 °S. This high-altitude peak shows similarities in location during the first half of southern fall and the second half of southern winter with its counterpart over the north polar latitudes. Local time distribution of the retrieved vertical profiles of O_3 show that the high-altitude peaks in the north and south polar regions show a lack of variability in magnitude and location with respect to the variations in the local time. In contrast, no high-altitude peak of ozone was observed at equatorial latitudes at any time throughout the martian year.

Given how complicated it is to model the vertical distribution of ozone, the GEM-Mars model results are able to very well reproduce the general behavior of the high-altitude peak of ozone when compared to the UVIS O_3 retrievals. In particular, the GEM-Mars predicts the presence of high-altitude peaks of ozone at polar latitudes around the beginning of northern spring and autumn and at the same altitudes observed by UVIS retrievals. In addition, the GEM-Mars model results accurately predict that the high-altitude peak in the south polar latitudes is more prominent compared to its counterpart in the north and that it persists for more than two seasons on Mars. Differences include higher GEM-Mars ozone abundance in the high-altitude peaks, reaching a factor of 5 in some occasions, leading to a larger vertical extent in the atmosphere than what is observed by UVIS. GEM-Mars also predicts the presence of a high-altitude peak of ozone around northern summer between latitudes 30 and 60 °N that is not observed as an independent layer by UVIS.

We demonstrated that all the differences between GEM-Mars and the observations can be attributed to under-or overestimates of water vapor abundances in the model, which were already presented and discussed in previous works (Daerden et al., 2019; Aoki et al., 2019). The strong anti-correlation between ozone and water vapor caused by the action of HO_x chemistry resulting from water vapor photolysis, can then readily explain the biased in ozone. Improvements in the simulation of the water cycle envisaged in the GEM-Mars model may improve the simulation of water vapor profiles in the future and improve the comparisons with the ozone profiles presented here.

Acknowledgements

This work was supported by NASA's Mars Program Office under WBS 604796, "Participation in the TGO/NOMAD Investigation of Trace Gases on Mars." The NOMAD experiment is led by the Royal Belgian Institute for Space Aeronomy (IASB-BIRA), assisted by Co-PI teams from Spain (IAA-CSIC), Italy (INAF-IAPS), and the United Kingdom (Open University). This project acknowledges funding by the Belgian Science Policy Office (BELSPO), with the financial and contractual coordination by the ESA Prodex Office (PEA 4000103401, 4000121493), by Spanish Ministry of Science and Innovation (MCIU) and by European funds under grants PGC2018-101836-B-I00 and ESP2017-87143-R (MINECO/FEDER), as well as by UK Space Agency through grants ST/V002295/1, ST/P001262/1, ST/S00145X/1 and ST/V005332/1 and Italian Space Agency through grant 2018-2-HH.0. This work was supported by the Belgian Fonds de la Recherche Scientifique – FNRS under grant number 30442502 (ET_HOME). The IAA/CSIC team acknowledges financial support from the State Agency for Research of the Spanish MCIU through the 'Center of Excellence Severo Ochoa' award for the Instituto de Astrofísica de Andalucía (SEV-2017-0709). US investigators were supported by the National Aeronautics and Space Administration. Canadian investigators were supported by the Canadian Space Agency. The TGO data are publicly available through the European Space Agency's Planetary Science Archive (archives.esac.esa.int/psa/) with additional access to NOMAD data through the PI institute (nomad.aeronomie.be). The results retrieved from the NOMAD/UVIS observations here will be publicly available at the permanent repository Mendeley (link TBD) by the time the manuscript is considered for publication.

References

Aoki, S., Vandaele, A. C., Daerden, F., Villanueva, G. L., Liuzzi, G., Thomas, I. R., et al., (2019). Water vapor vertical profiles on Mars in dust storms observed by TGO/NOMAD. *Journal of Geophysical Research: Planets*, 124, 3482–3497. https://doi.org/10.1029/2019JE006109

Barth, C.A., Hord, C.W., (1971). Mariner ultraviolet spectrometer: topography and polar cap. *Science*, 173(3993):197-201. doi:10.1126/science.173.3993.197.

Barth, C.A., Hord, C.W., Stewart, A.I., Lane, A.L., (1972). Mariner 9 ultraviolet spectrometer experiment: initial results. *Science*, 175(4019):309-312. doi:10.1126/science.175.4019.309.

Barth, C.A., Hord, C.W., Stewart, A.I., Lane, A.L., Dick, M.L., Anderson, G.P., (1973). Mariner 9 ultraviolet spectrometer experiment: seasonal variation of ozone on Mars. *Science*, 179(4075):795-796. doi:10.1126/science.179.4075.795.

Blamont, J.E., Chassefière, E., (1993). First Detection of Ozone in the Middle Atmosphere of Mars from Solar Occultation Measurements, *Icarus*, 104, 2, 324-336, https://doi.org/10.1006/icar.1993.1104.

Clancy, R.T., and H. Nair, (1996). Annual (perihelion–aphelion) cycles in the photochemical behavior of the global Mars atmosphere. *J. Geophy. Res*. 101(E5), 12,785–12,790.

Clancy, R.T., Wolff, M. J., James, P. B., Smith, E., Billawala, Y. N., Lee, S. W., and Callan, M., (1996). Mars ozone measurements near the 1995 aphelion: Hubble space telescope ultraviolet spectroscopy with the faint object spectrograph, *J. Geophys. Res.*, 101 (E5), 12777– 12783, doi:10.1029/96JE0083.

Clancy, R.T., Wolff, M.J., Lefèvre, F., Cantor, B.A., Malin, M.C., Smith M.D., (2016). Daily global mapping of Mars ozone column abundances with MARCI UV band imaging *Icarus*, 266, pp. 112-133, 10.1016/j.icarus.2015.11.016

Daerden, F., Neary, L., Viscardy, S., García Muñoz, A., Clancy, R.T., Smith, M.D., Encrenaz, T., Fedorova, A., (2019). Mars atmospheric chemistry simulations with the GEM-Mars general circulation model, *Icarus*, 326, 197-224, https://doi.org/10.1016/j.icarus.2019.02.030.

Espenak, F., M. J. Mumma, T. Kostiuk, and D. Zipoy, (1991). Ground-based infrared measurements of the global distribution of ozone in the atmosphere of Mars, *Icarus*, 92, 252–262.

Fast, K., Kostiuk, T., Espenak, F., Annen, J., Buhl, D., Hewagama, T., Schmülling, F., (2006). Ozone abundance on Mars from infrared heterodyne spectra. I. Acquisition, retrieval, and anticorrelation with water vapor. *Icarus* 181, 419–431.

Goldman, A., & Saunders, R., (1979). Analysis of atmospheric infrared spectra for altitude distribution of atmospheric trace constituents I. Method of analysis. *Journal of Quantitative Spectroscopy and Radiative Transfer*, 21(2), 155–161. doi: 10.1016/0022-4073(79)90027-X.

Guzewich, S. D., Lemmon, M., Smith, C. L., Martínez, G., de Vicente-Retortillo, Á., Newman, C. E., et al., (2019). Mars Science Laboratory observations of the 2018/Mars year 34 global dust storm. *Geophys. Res. Letters*, 46,71–79. https://doi.org/10.1029/2018GL080839

Lebonnois, S., Qúemerais, E., Montmessin, F., Lefèvre, F., Perrier, S., Bertaux, J-L, and Forget, F., (2006. Vertical distribution of ozone on Mars as measured by SPICAM/Mars express using stellar occultations; *J. Geophys. Res. Planets* 111(E9), https://doi.org/10.1029/2005JE002643.

Lefèvre, F., Lebonnois, S., Montmessin, F., and Forget, F., (2004). Three-dimensional modeling of ozone on Mars, J. *Geophys. Res.*, 109, E07004, doi:10.1029/2004JE002268.

Lefèvre, F. & Bertaux, Jean-Loup & Perrier, S. & Lebonnois, S. & Korablev, O. & Fedorova, Anna & Montmessin, F. & Forget, F., (2007). The Martian Ozone Layer as Seen by SPICAM/Mars-Express. *LPI Contributions*.

Malin, M.C., Calvin W., Clancy R.T., Haberle R.M., James P.B., Lee S.W., Thomas P.C., Caplinger M.A., (2001). The Mars Color Imager (MARCI) on the Mars climate orbiter *J. Geophys. Res. Planets*, 106 (2001), pp. 17651-17672, 10.1029/1999JE001145.

Malin, M.C., Calvin, W.M., Cantor, B.A., Clancy, R.T., Haberle, R.M., James, P.B., Thomas, P.C., Wolff, M.J., Bell, J.F., Lee, S.W., (2008). Climate, weather, and north polar observations from the Mars Reconnaissance Orbiter Mars Color Imager *Icarus*, 194, pp. 501-512, 10.1016/j.icarus.2007.10.016

Markwardt, C.B., (2009). Non-linear least-squares Fitting in IDL with MPFIT. In: Bohlender, D.A., Durand, D., Dowler, P. (Eds.), *Astron. Data Anal. Softw. Syst*. XVIII, p. 251. 0902.2850.

Montmessin, F., Lefèvre, F., (2013). Transport-driven formation of a polar ozone layer on Mars. *Nature Geoscience* 6, 930–933. https://doi.org/10.1038/ngeo1957

Montmessin, F., et al., (2017). SPICAM on Mars Express: a 10 year in-depth survey of the Martian atmosphere *Icarus*, 297, pp. 195-216.

Navarro, T., Madeleine, J.-B., Forget, F., Spiga, A., Millour, E., Montmessin, F., Määttänen, A., (2014). Global climate modeling of the Martian water cycle with improved microphysics and radiatively active water ice clouds. *J. of Geophys. Res. Planets* 119, 1479–1495. https://doi.org/10.1002/2013JE004550.

Neary, L., Daerden, F., (2018). The GEM-Mars general circulation model for Mars: description and evaluation. *Icarus* 300, 458–476. https://doi.org/10.1016/j.icarus.2017.09.028.

Neary, L., Daerden, F. S. Aoki J. Whiteway R. T. Clancy M. Smith S. Viscardy J.T. Erwin I. R. Thomas G. Villanueva G. Liuzzi M. Crismani M. Wolff S. R. Lewis J. A. Holmes M. R. Patel M. Giuranna C. Depiesse A. Piccialli S. Robert L. Trompet Y. Willame B. Ristic A. C. Vandaele, (2020). Explanation for the Increase in High-Altitude Water on Mars Observed by NOMAD During the 2018 Global Dust Storm. *Geophys. Res. Lett.*, 47, 70094-8276. https://doi.org/10.1029/2019GL084354

Novak, R.E, Mumma, M.J., DiSanti, M.A., Dello Russo, N., (2002). Mapping of ozone and water in the atmosphere of Mars near the 1997 aphelion. *Icarus*, 158, pp. 14-23. https://doi.org/10.1006/icar.2002.6863

Noxon, J. F., W. A. Traub, N. P. Carleton, and P. Connes, (1976). Detection of O_2 dayglow emission from Mars and the martian ozone abundance. *Astrophy. J.* 207, 1025–1035.

Perrier, S., Bertaux, J. L., Lefèvre, F., Lebonnois, S., Korablev, O., Fedorova, A., and Montmessin, F., (2006). Global distribution of total ozone on Mars from SPICAM/MEX UV measurements, *J. Geophys. Res.*, 111, E09S06, doi:10.1029/2006JE002681.

Patel, M., Antoine, P., Mason, J., Leese, M., Hathi, B., Stevens, A., Dawson, D., Gow, J., Ringrose, T., Holmes, J., Lewis, S., Beghuin, D., Van Donink, P., Ligot, R., Dewandel, J., Hu, D., Bates, D., Cole, R., Drummond, R., Thomas, I., Depiesse, C., Neefs, E., Equeter, E., Ristic, B., Berkenbosch, S., Bolsée, D., Willame, Y., Vandaele, A., Lesschaeve, S., De Vos, L., Van Vooren, N., Thibert, T., Mazy, E., Rodriguez-Gomez, J., Morales, R., Candini, G., Pastor-Morales, M., Sanz, R., Aparicio del Moral, B., Jeronimo-Zafra, J., Gómez-López, J., Alonso-Rodrigo, G., Pérez-Grande, I., Cubas, J., Gomez-Sanjuan, A., Navarro-Medina, F., BenMoussa, A., Giordanengo, B., Gissot, S., Bellucci, G., and Lopez-Moreno, J., (2017). NOMAD spectrometer on the ExoMars trace gas orbiter mission: part 2—design, manufacturing, and testing of the ultraviolet and visible channel, *Appl. Opt*. 56, 2771-2782.

Patel, M.R., Sellers, G., Mason, J.P., Holmes, J.A., Brown, M.A.J., Lewis, S.R., Rajendran, K., Streeter, P.M., Marriner, C., Hathi, B.G., Slade, D.J., Leese, M.R., Wolff, M.J., Khayat, A. SJ., Smith, M.D., Clancy, R.T., Aoki, S., Piccialli, A., Vandaele, A. C., Daerden, F., Thomas, I.R., Ristic, B., Willame, Y., Depiesse, C., Bellucci, G., and Lopez-Moreno, J.-J. The vertical distribution of ozone on 1 Mars in MY34/35 from ExoMars TGO/NOMAD observations. *Journal of Geophysical Research- Planets*, this issue.

Sander, S.P. & Abbatt, Jonathan & Barker, John & Burkholder, J.B. & Friedl, R.R. & Golden, D.M. & Huie, Robert & Kurylo, Michael & Moortgat, Geert & Orkin, Vladimir & Wine, Paul., (2011). *Chemical Kinetics and Photochemical Data for Use in Atmospheric Studies*, Evaluation No. 17.

Shaposhnikov, D. S., Rodin, A. V., Medvedev, A. S., Fedorova, A. A., Kuroda, T., & Hartogh, P., (2018). Modeling the hydrological cycle in the atmosphere of Mars: Influence of a bimodal size distribution of aerosol nucleation particles. *Journal of Geophysical Research: Planets*, 123, 508– 526. https://doi.org/10.1002/2017JE005384

Smith, M. D., Daerden, F., Neary, L., Khayat, A, (2018). The climatology of carbon monoxide and water vapor on Mars as observed by CRISM and modeled by the GEM-Mars general circulation model, *Icarus*, 301, 117-131.

Smith, M. D., (2019). THEMIS Observations of the 2018 Mars Global Dust Storm. Journal of *Geophysical Research: Planets*, 124, 2929– 2944. https://doi.org/10.1029/2019JE006107

Vandaele, A., Willame, Y., Depiesse, C., Thomas, I., Robert, S., Bolsée, D., Patel, M., Mason, J., Leese, M., Lesschaeve, S., Antoine, P., Daerden, F., Delanoye, S., Drummond, R., Neefs, E., Ristic, B., Lopez-Moreno, J., Bellucci, G., and Nomad Team, (2015). Optical and radiometric models of the NOMAD instrument part I: the UVIS channel, *Opt. Express*, 23, 30028-30042.

Vandaele, A.C., Lopez-Moreno, J., Patel, M.R. et al., (2018). NOMAD, an Integrated Suite of Three Spectrometers for the ExoMars Trace Gas Mission: Technical Description, Science Objectives and Expected Performance, *Space Sci. Rev.* 214, 80, https://doi.org/10.1007/s11214-018-0517-2

Willame, Y., Vandaele, A.C., Depiesse, C., Lefevre, F., Letocart, V., Gillotay, D., Montmessin, F., (2017). Retrieving cloud, dust and ozone abundances in the Martian atmosphere using SPICAM/UV nadir spectra. *Planet. Space Sci*., 142, pp. 9-25.

Wolff, M. J., Lopez-Valverde, M., Madeleine, J.-B., Wilson, R. J., Smith, M. D., Fouchet, T., & Delory, G. T., (2017). Radiative Process: Techniques and Applications. In R. M. Haberle et al. (Eds.), The atmosphere and climate of Mars (p. 76-105). *Cambridge University Press*. doi: 10.1017/9781139060172.00